IMPROVING MANUFACTURABILITY AND REDUCING CRACKING IN ADDITIVELY MANUFACTURED TUNGSTEN ALLOYS

THESIS

Christopher P. Fassio, Captain, USAF

AFIT-ENY-MS-21-M-299

DEPARTMENT OF THE AIR FORCE
AIR UNIVERSITY

AIR FORCE INSTITUTE OF TECHNOLOGY

Wright-Patterson Air Force Base, Ohio

AFIT-ENY-MS-21-M-299

IMPROVING MANUFACTURABILITY AND REDUCING CRACKING IN ADDITIVELY MANUFACTURED TUNGSTEN ALLOYS

THESIS

Presented to the Faculty

Department of Aeronautical and Astronautical Engineering

Graduate School of Engineering and Management

Air Force Institute of Technology

Air University

Air Education and Training Command

in Partial Fulfillment of the Requirements for the

Degree of Master of Science in Aeronautical Engineering

Christopher P. Fassio, B.S.M.E.

Captain, USAF

March 18, 2021

AFIT-ENY-MS-21-M-299

IMPROVING MANUFACTURABILITY AND REDUCING CRACKING IN ADDITIVELY MANUFACTURED TUNGSTEN ALLOYS

THESIS

Christopher P. Fassio, B.S.M.E.
Captain, USAF

Committee Membership:

Ryan Kemnitz, Ph.D.
Chair

Larry Burggraf, Ph.D.
Member

Carl Hartsfield, Ph.D.
Member

Abstract

Additively manufactured tungsten suffers from low (<95%) densities due to high concentrations of microcracks as the printed layers cool past tungsten's high ductile to brittle transition temperature. In this study, tungsten-rhenium and tungsten rhenium hafnium carbide (WReHfC) compositions were evaluated on density and tensile strength. In addition to varying the compositions of each alloy, printing parameters and post-processing methods were also compared. Using an MLab 200R Cusing, print parameters including the laser scan strategy, hatch spacing, scan speed, laser power, and print bed material were varied for alloy compositions. Post-processing techniques of the WRe compositions included hot isostatic pressing and hydrogen annealing treatments. In particular, two combinations achieved high density (>97%) indicating a reduction in microcracking: W25Re which underwent H annealing, and W25Re1HfC as-printed. In both cases the mechanism was likely oxygen impurities being scavenged, either by hydrogen or carbon. The H annealed W25Re tensile bar achieved a maximum 701 MPa room temperature ultimate tensile strength. Scanning electron microscope images of the annealed W25Re and the as-printed W25Re1HfC show no microcracks. This was further confirmed on the W25Re1HfC using Focused Ion Beam imaging techniques. However, the reduction in microcracking in the latter led to a buildup in thermal stresses during printing, causing both lifting from the print bed, and macro sized cracks through the printed part approximately every 5mm in print height. Lifting was reduced in the W25Re1HfC and eliminated in the W25Re by using a copper build plate.

Table of Contents

Page

List of Figures

List of Tables

List of Acronyms

AM	additively manufactured
BCC	Body-Centered Cubic
CT	computed tomography
Cu	copper
DBTT	Ductile to Brittle Transition Temperature
DED	direct energy depositoin
EBM	electron beam melting
EBSD	Electron Backscatter Diffraction
EDM	Electrical Discharge Machining
HCP	Hexagonal Close-Packed
HIP	Hot Isostatic Pressing
HSS	High Speed Steels
LPBF	laser powder bed fusion
MRI	Magnetic Resonance Imaging
PBF	powder bed fusion
SEM	scanning electron microscope
SLS	selective laser sintering
TD	theoretical density
UTS	ultimate tensile strength
W	Watt (when preceded by a number)
W	tungsten
W25Re	75% by weight tungsten, 25% rhenium
W25Re1HfC	74% by weight tungsten, 25% rhenium 1% hafnium carbide
W3C and WC	Tungsten Carbides

WRe	tungsten rhenium
WReHfC	tungsten rhenium hafnium carbide

IMPROVING MANUFACTURABILITY AND REDUCING CRACKING IN ADDITIVELY MANUFACTURED TUNGSTEN ALLOYS

I. Introduction

tungsten (W) is what is known as a refractory metal, joining niobium, molybdenum, tantalum and rhenium in that category [4]. The term refractory denotes these metals' resistance to radiation, corrosion, and heat. All of them have high melting temperatures, with tungsten being the highest at $\sim$ 3422 deg C and rhenium second at $\sim$ 3185 deg C. Tungsten is very hard, extremely dense at 19.246 g/cm^3, and has a high thermal conductivity and low vapor pressure [4, 5]. Early uses of tungsten made use of the high melting point in the form of filaments for incandescent light bulbs [6]. Modern uses of tungsten are dominated by tungsten carbide tools due to their hardness and ability to withstand the extreme heat of cutting. Innovative new techniques in manufacturing can be used to harness old and new material systems alike to allow advances in aerospace, medical, and military applications. One such technique is additive manufacturing, commonly known as 3D Printing.

1.1 Additive Manufacturing

Additive manufacturing is a burgeoning new field [7] with additive metal manufacturing even newer. Weight saving designs, previously impossible geometries, and rapid prototyping are benefits of additive manufacturing. However, tungsten's properties that make it valuable as a material also bring numerous challenges [6,8] with additive manufacturing processes. additively manufactured (AM) tungsten is prone to large amounts of microcracking and maximum densities of bulk tungsten are around 96%

of the theoretical density (TD) of pure tungsten [2, 8–10]. These shortcomings relegate AM tungsten to nonstructural applications like collimators and radiation shields in medical imaging devices such as computed tomography (CT) scans and Magnetic Resonance Imaging (MRI) machines. Manufacturing advances with AM tungsten are necessary to harness tungsten's unique properties in demanding structural aerospace applications.

1.2 Research Outline

1.2.1 Problem Statement

Current AM tungsten parts are limited in their usefulness [6] due mainly to the lower density and higher brittleness than traditionally manufactured tungsten [8, 9]. However, tungsten's properties, including high melting temperature, low x-ray permeability, moderate thermal and high electrical conductivity, make it ideal for military and civilian applications. Additively manufactured space power systems [11], high temperature heat exchangers with high surface areas [12], nuclear shielding equipment [13], and hypersonic components [14] are all potential candidates for additively manufactured tungsten parts with comparative mechanical properties to traditionally manufactured pieces.

1.2.2 Research Questions

tungsten rhenium (WRe) and tungsten rhenium hafnium carbide (WReHfC) alloys are hypothesized to be more amenable to the AM process and produce dense, structurally sound parts based on existing tungsten metallurgy [4,6,9,10,15–18]. This hypothesis was steered by the following research questions:

- What specific alloy compositions of WRe and WReHfC reduce cracking and increase density compared to pure tungsten?

- Which WRe and WReHfC printing parameters on a 200 Watt (when preceded by a number) (W) laser powder bed fusion (LPBF) machine will reduce cracking and increase density compared to pure tungsten prints?
- What effect do heat treatments have on AM tungsten alloys?
- What are the causal chemical mechanisms for any improvements or detriments to the print quality?
- How do quantitative and qualitative part quality manifest in the mechanical properties of AM tungsten alloys?

1.2.3 Scope and Methodology

This research investigated tungsten alloy compositions, print parameters, and post-processing heat treatment techniques to suppress microcracking and improve the mechanical properties of additively manufactured tungsten. The two specific alloy compositions investigated are 75% by weight tungsten, 25% rhenium (W25Re) and 74% by weight tungsten, 25% rhenium 1% hafnium carbide (W25Re1HfC). Crack suppression was determined quantitatively by density measurements of printed material and qualitatively by scanning electron microscope (SEM) imaging. Microstructure was examined using the Electron Backscatter Diffraction (EBSD) analysis module of the SEM. Mechanical properties studied included the ultimate tensile strength via tensile testing and Vickers hardness. The initial print parameters were derived from previous studies [2, 10] of pure tungsten and adapted to W25Re and W25Re1HfC.

1.2.4 Assumptions

While the print conditions in this study were controlled as much as possible, many variations exist that are considered negligible. Effects due to build plate lo-

cation, recycled vs freshly mixed powder, variations in weighted percentage of each alloy composition, oxygen content fluctuations in the build chamber or other random effects due to handling were assumed negligible in their effect. Primary parameters assumed to affect additively manufactured parts were powder composition, AM machine process parameters, and heat treatments. Each heat treatment of the additively manufactured parts was assumed to be a consistent, repeatable process. If an alloy percentage is given, it is assumed to be by weight unless noted otherwise.

1.2.5 Near Term Impacts

Studies on the densification and strengthening of additively manufactured tungsten alloys can provide insight into the mechanisms of crack suppression and densification. Rhenium is expensive, but known to increase ductility of tungsten at low temperatures and increase strength at high temperatures [6, 11]. By studying alloys, AM processing parameters, and heat treatment post-processing, reducing or eliminating the need for rhenium may prove possible to create low-cost additively manufactured tungsten structures.

II. Background and Related Work

2.1 Tungsten

Tungsten's first recorded discovery was in Medieval tin mines, where it's mineral form lowered tin yield with a foamy substance when melting. This earned it the name "wolf's spittle", or Wolfram for "wolf's foam" in German. Wolfram is the modern German word for tungsten and the chemical symbol for tungsten is W [4]. From decorative jewelry to high energy kinetic penetrators for the military, to radiation shielding for medical X-rays and space applications, tungsten has a wide variety of uses. One field where tungsten finds particular utilization is the manufacturing and engineering industries. High Speed Steels (HSS) and Tungsten Carbides (W3C and WC) are used extensively in tooling designed to cut, drill or mill. They increase the hardness, the high-temperature hardness, and wear resistance of the tools [19]. Tungsten is second only to vanadium as the most effective carbide-forming element in tool steels [4]. However, many of these desirable physical properties can have unfortunate side effects.

2.1.1 Tungsten Metallurgy

Tungsten's high melting point made it famously useful as the filament material in the incandescent light bulb. Tungsten has other useful material properties but is often limited by its high Ductile to Brittle Transition Temperature (DBTT). The DBTT is the temperature below which a material is brittle, and above which is ductile. "Pure" or single crystal tungsten is ductile at room temperatures and lower. Tungsten's alpha phase is the most common; this has a DBTT which rises depending on the grain size [1], typically between 200-300 deg C [1,4,20]. See Figure 1 in Section 2.1.2 for the relationship between grain size and DBTT. The grain size itself is af-

fected by manufacturing technique and is temperature dependent. The high DBTT of tungsten presents difficulties in manufacturing, with industry favoring Powder Metallurgy, Powder Injection Molding, Electrical Discharge Machining (EDM) [21], and other high temperature, high pressure methods.

Room temperature tungsten atoms naturally arrange themselves into a Body-Centered Cubic (BCC) crystal lattice structure. Tungsten is dominated by intergranular fracture [20]. This is a fracture through the separation of the grains along the grain boundaries. The brittle nature of tungsten is due to two primary reasons: a low intergranular fracture energy and the previously mentioned high DBTT [4]. Dislocation motion is impeded more in BCC metals than Hexagonal Close-Packed (HCP) or other close-packed metallic crystals [4, 22]. The low intergranular fracture energy is made even worse by interstitial impurities [4, 20].

The interstitial impurities are imbued in tungsten by its high temperature manufacturing processes. The high temperature increases the solubility for elements like hydrogen, oxygen, silicon, carbon, potassium and phosphorus [6]. These common elements cannot easily bond with room temperature tungsten, but penetrate the high temperature raw tungsten material. While cooling, the lower temperature low solubility shifts the impurities to the grain boundaries, thus exacerbating the already low intergranular fracture energy [20]. As such, tungsten's mechanical properties are highly dependent on the individual and combination of impurities contained within the piece [4]. Because of this dependence, material properties are often given as ranges and curves rather than specific values.

Welding tungsten is also influenced by the impurities. Welding must be done in either an inert gas or a vacuum, and the equipment must be able to bear the high temperatures needed to melt tungsten [18]. Welding in ambient atmosphere introduces too many impurities into the tungsten, which causes cracking. However,

rhenium is often used in tungsten welding to reduce cracking.

2.1.2 Tungsten Rhenium and Tungsten Rhenium Hafnium Carbide Systems

Rhenium itself is a refractory metal with the second-highest melting point at about 3180 deg C. It would probably be more widespread in use if it was more widespread in availability. Rhenium is extremely scarce and shares some of the difficulties to manufacture with tungsten. Both factors drive up the cost of rhenium [23]. In 1990 the cost of rhenium was around $1,500 US per kilogram. The commercial supplier of rhenium powder for this research, Rhenium Alloys based in Cleveland OH, provided rhenium powder at a cost of approximately $3,000 per kg. Rhenium shares many attributes to tungsten, including corrosion, radiation, and thermal resistance [23]. Three key differences are that rhenium does not form carbides, it is ductile at room temperatures (even down to approximately 0 K), and its crystal structure is an HCP form [23]. When alloyed with tungsten many of the benefits of both emerge, while reducing the disadvantages of either. The main advantage tungsten gains when alloyed with rhenium is a lower DBTT [1, 4, 6, 24–31]. Tungsten alloys with as little as 1 at% Re show a noticeable drop in DBTT [27]. The effect increases up to the solubility limit of rhenium in tungsten around W-27 wt% Re [1, 4]. Figure 1 shows the DBTT vs. grain size for both pure polycrystalline tungsten and W-24/26 at% Re:

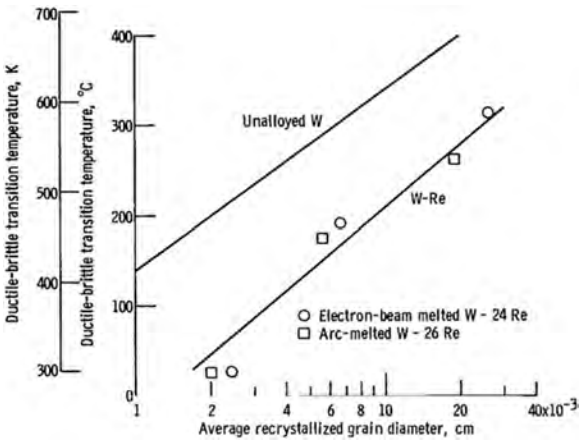

Figure 1. Bend transition temperature for recrystallized tungsten and tungsten rhenium alloys as a function of grain size [1]

The smaller grain size typically results in stronger tungsten [6, 25, 32]. Tungsten can be cold-rolled or similarly mechanically worked to create these smaller grains, but alloying with rhenium also reduces grain size [29]. Various alloys of WRe have drastically different effects on the yield stress as shown in Table 1. Room temperature W25Re is shown to have an ultimate strength of 1044 MPa [3].

Material Condition and Temperature	E (GPa)	Max. Stress (MPa)	0.2% Offset Yield Strength (MPa)	Strain at Max Stress (% Elongation)
RT HIP W25%Re	457	1044	973	1.87%
RT Swaged W25%Re	441	1428	1278	5.15%
RT Swaged W24.5%Re2%HfC	437	1344	1269	2.40%
RT Extruded W24.5%Re2%HfC	418	1413	1254	6.29%
1,371°C HIP W25%Re	258	466	298	10.69%
1,371°C Swaged W25%Re	222	546	383	6.64%
1,371°C Swaged W24.5%Re2%HfC	293	760	602	10.14%
1,371°C Extruded W24.5%Re2%HfC	301	687	553	9.22%
1,926°C HIP W25%Re	132	143	90	6.08%
1,926°C Swaged W25%Re	132	140	90	5.12%
1,926°C Swaged W24.5%Re2%HfC	82	281	138	7.90%
1,926°C Extruded W24.5%Re2%HfC	110	273	148	5.65%

*Tensile tests were performed using controlled stress rate testing at 30 ksi/min (207 MPa/min).

Table 1. Mechanical Testing Results:* Summary and Comparison by Temperature and by Processing Method [3]

2.2 Metal Additive Manufacturing

Additive manufacturing uses a layer build-up approach to create parts from 3D models [33, 34], as opposed to cutting away material from a pre-made stock of metal using a mill, lathe or other subtractive manufacturing tools. Additive manufacturing of metals allows for parts that were not previously manufacturable using casting, powder sintering, forging, or subtractive methods [34]. However, the methods used to additively manufacture metal parts determine their viability and performance. Additive manufacturing was invented in 1986 [7] by Chuck Hull, and is still quite a young field; different organizations have different classifications for additive methods. Additive manufacturing methods can be characterized by either their bonding method or raw material feedstock required, or both. ASTM International [35] has seven categories of additive manufacturing, based on bonding method. Of these, only four: material extrusion, powder bed fusion, direct energy deposition, and sheet lamination are commonly used in metal manufacturing. However, material extrusion and sheet lamination techniques both suffer from poor surface finish [33].

2.2.1 Printing Technologies

The present discussion will focus on powder bed fusion (PBF) and direct energy depositoin (DED) additive manufacturing methods for metals. Powder bed fusion processes are all very similar in execution. First, the 3D model is sliced using software to divide the part into 2D stacking layers. Layers may also be programmatically generated via scripts. Once the additive machine has each layer's information, a coater arm spreads metal powder from a powder chamber onto a build plate. Energy is applied to the powder, creating a solid layer with a similar layer height as the powder size. The build plate is lowered, the coater arm wipes powder again, and the layers build to the completed part. Powder bed fusion methods differ in whether

they fully melt the powder, or merely heat it to sintering, and in how they apply the heat energy. selective laser sintering (SLS) uses a focused laser to heat the powder to sintering. uses a focused laser to heat the powder to melting, usually creating denser parts with bulk properties closer to traditionally manufactured material than SLS. electron beam melting (EBM) is identical to SLM, but uses an electron gun instead of a laser. In the powder bed methods, the powder feedstock is stationary, while the laser or electron beam energy is directed by a moving mirror to the area to solidify. In DED the 3D part model is again reduced to layer instructions. However, in DED, the feedstock powder or wire is fed through a nozzle and melted. The nozzle is mounted on a gantry that positions the melted material onto the area of the build plate.

2.2.2 Metal Powder

The metal powder is the fundamental building block for PBF processes. Metal powder use in metalworking has a history long predating additive manufacturing. Ancient Indian and Incan civilizations used powderized forms of iron to create sponge iron as far back as 3000 BCE. This was further forged into tools [36]. Tungsten powder metallurgy was used to create filaments for incandescent lights in the 19th century. Due to the high melting temperature, tungsten powder is typically vacuum sintered with dopants, such as nickel, to achieve high densification at less extreme temperatures. Hot Isostatic Pressing (HIP) uses high temperature non-reactive gas, typically argon, to fuse the metal powder at lower temperatures than even sintering.

Modern metal powders are typically manufactured using plasma or gas atomization [37]. Plasma atomization utilizes plasma torches to vaporize metal wire in a vacuum, which then cools into spherical droplets. Gas atomization uses pressurized inert gas such as argon to disperse a melted metal. Figure 2 shows SEM images of

pure tungsten powder at 1000x and 5000x magnification.

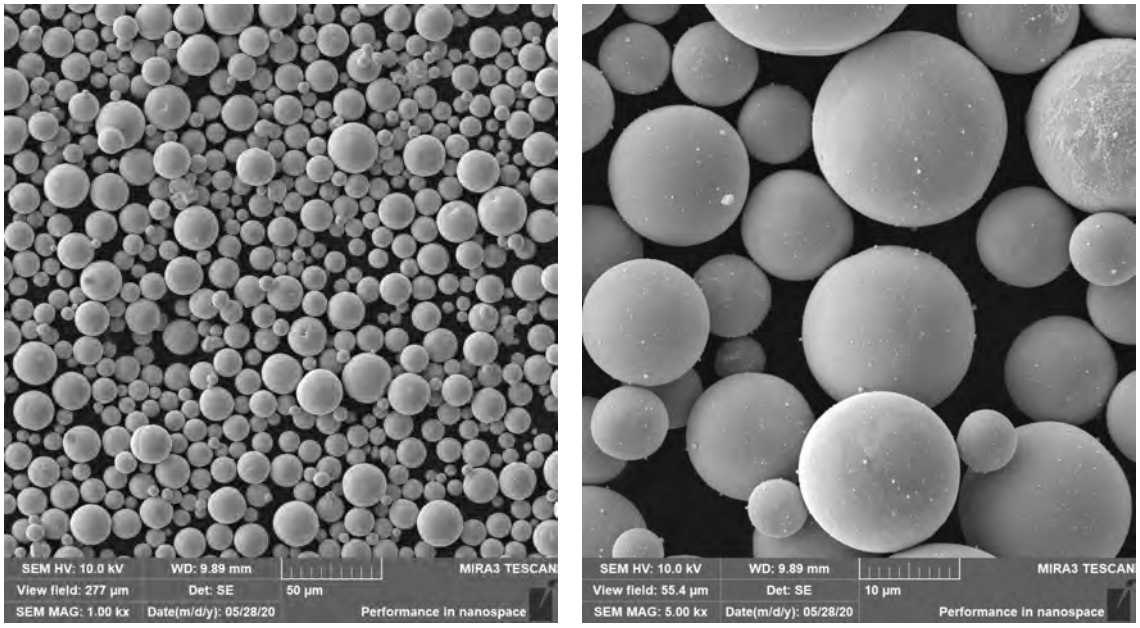

(a) W Powder 1000x (b) W Powder 5000x

Figure 2. W Powder

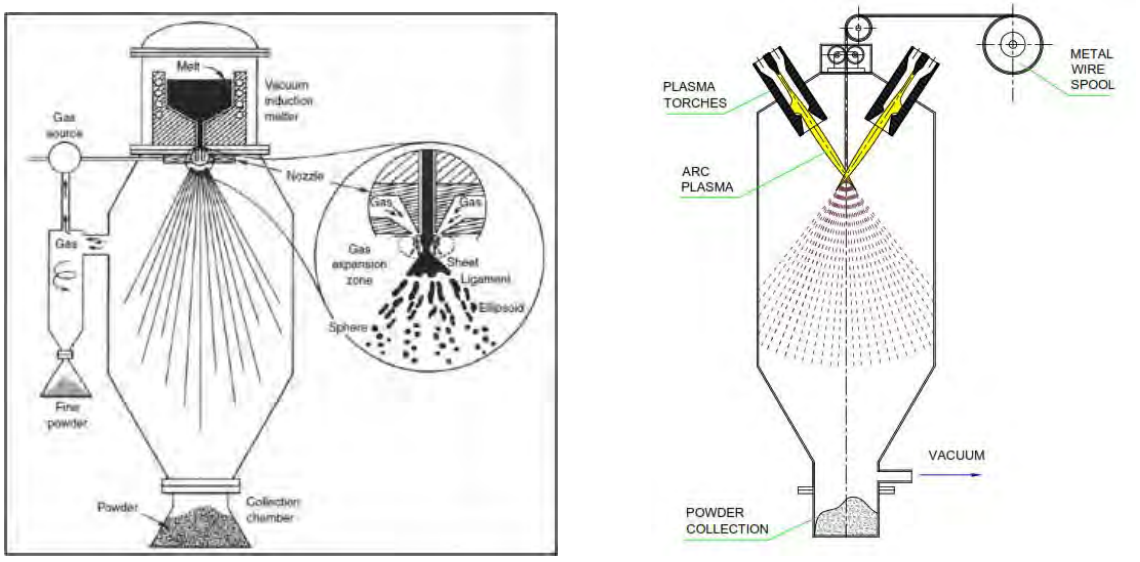

(a) Gas Atomization [38] (b) Plasma Atomization [39]

Figure 3. Atomization Schematics to Manufacture Metal Powders

2.2.3 Printing Parameters

The PBF processing or printing parameters are user controlled to refine the process to create dense, useful materials. The present work used a Concept Laser Mlab 200R SLM machine. The Mlab Additive Manufacturing machine and Magics slicing software allow the user to adjust many processing parameters, including laser power, laser scan speed, hatch spacing, and layer thickness. These parameters "are adjusted such that a single melt vector can fuse completely with the neighbouring melt vectors and the preceding layer" [40]. Powder size influences each of these parameters; too large a powder results in uneven melting, affecting the resolution of the print. In general, the smaller the powder, the better the flowability until sizes become small enough for Van der Waals forces to dominate. At this point flowability is hampered again [40]. Tan [16] notes about tungsten powder in particular: "Tungsten powder has an extremely high melting point and is prone to balling during SLM, thus selecting the correct layer thickness is crucial." Previous work on pure tungsten [2,10,16] found optimal powder layer thickness distances of 15-20 μm. Geometric fidelity to the 3D model occurred at hatch spacings of 25, 50 and 75 μm. The maximum laser power of 200 W for the Mlab printer proved optimal with laser speeds of 50-400 mm/s producing successful 10mm cube test prints. Laser scanning speeds of 100 mm/s produced high porosity surfaces with high cracking (Fig 4). The more optimal speed of 400 mm/s produced non-porous surfaces but still crack-ridden (Fig 5).

One way to normalize print settings between machines is to use the laser energy density, E_V [34]. This is calculated from the hatch spacing, h, the laser scan speed, V, the laser power, P, and powder bed thickness, t in Equation 1 below:

$$E_V = \frac{P}{Vht} \tag{1}$$

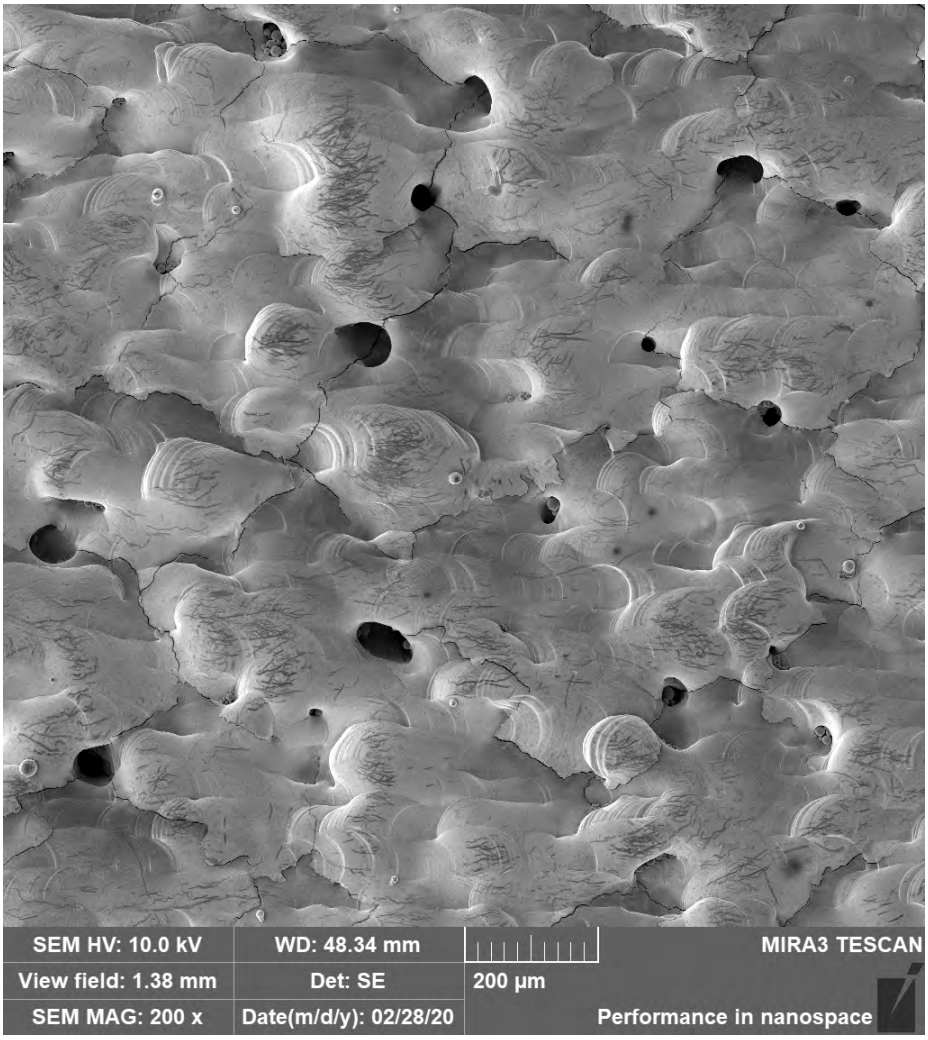

Figure 4. Pure W Printed Surface with 50 μm hatch, 100 mm/s laser speed, 15 μm layer height, and 200 W laser power [2]

2.2.4 Additive Manufacturing of Tungsten Alloys

While tungsten metallurgy is well understood [4], additive manufacturing of tungsten is still in its infancy. SLM printing of pure tungsten parts produces porous, crack-prone parts with maximum densities of 97% compared to bulk tungsten [41]. The highest densities of pure tungsten have been produced by cutting-edge additive manufacturing systems with the ability to reduce oxygen content in the build chamber to levels under 50 ppm vs other systems which maintain oxygen levels between 200-1000 ppm.. Tungsten alloys have also been processed by AM, including WTa [41],

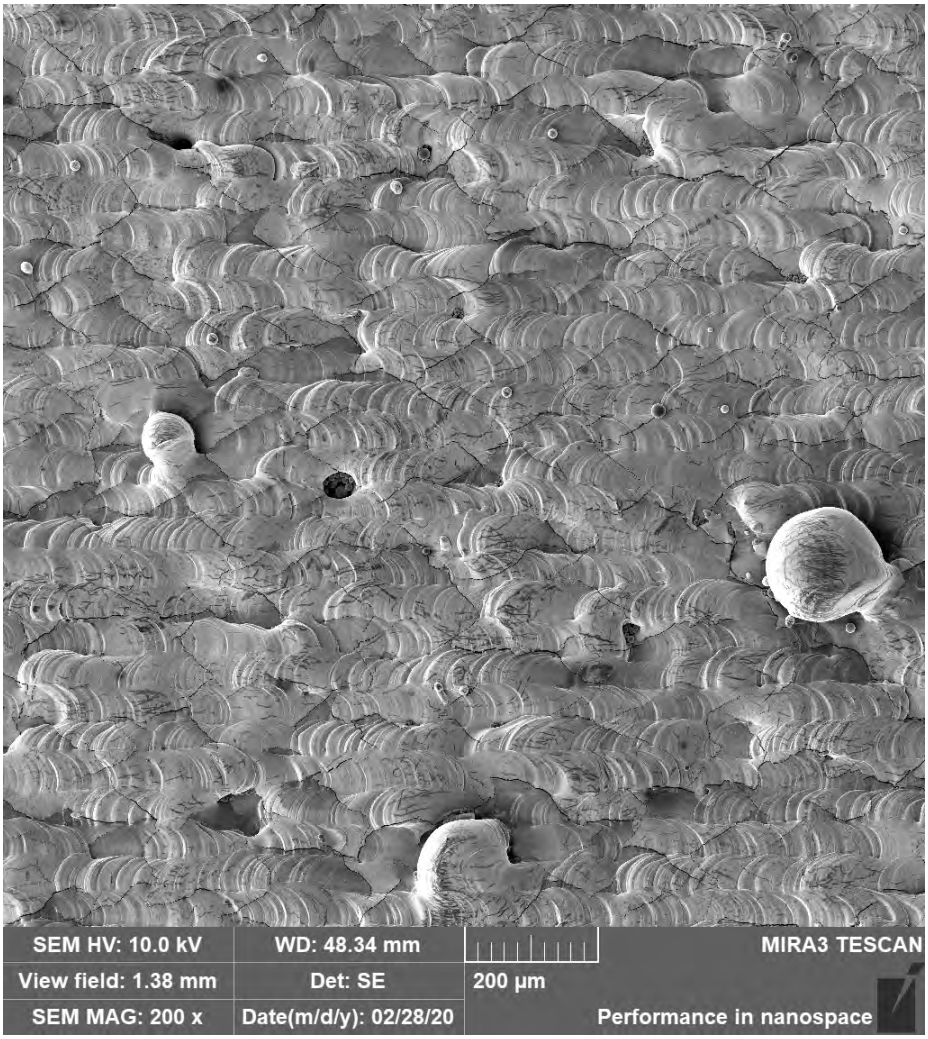

Figure 5. Pure W Printed Surface with 50 μm hatch, 400 mm/s laser speed, 15 μm layer height, and 200 W laser power [2]

W7Ni3Fe [42], and WZrC [17], but as of this writing, no research has been published on additively manufactured WRe or WReHfC alloys. Promising methods for reducing cracks include introducing carbides as secondary phase nanoparticles [17].

2.3 Post-Processing Heat Treatments

Heat treatmenting metal is a vital way to change the mechanical properties of the metal without altering its base alloy [43]. Essentially, heat treatments seek to change the microstructure of the material to effect macroscopic change in properties [43].

Heat treatments used as a metallurgical post-processing technique take a mostly finished metal product, apply heat, and cool the piece down again. What temperature to heat to, how long to hold at this temperature, how long to cool to room temperature or below, and how many stages of the previous parameters, are the main parameters in heat treatments. Rapid cooling, or quenching to strengthen steel, followed by a tempering and slow cooling to reduce brittleness are familiar to many. However, in AM, printed parts are typically less dense than their forged or cast counterparts.

The annealing process in AM has the end goal of increasing uniformity in the microstructure and removing impurities [4, 43]. Two traditional techniques adapted for AM parts are annealing in an oxygen reducing environment, such as hydrogen, and Hot Isostatic Pressing. Hydrogen annealing is traditional annealing in a hydrogen environment. The high temperature environment facilitates breaking of oxide bonds in the metal and promotes oxygen-hydrogen bonds. The metal piece is now more free of oxygen impurities and the microstructure becomes more homogeneous [43]. Hot Isostatic Pressing is a heat treatment process originally used to facilitate sintering in powder metallurgy. HIP treatments of AM parts are essentially high pressure annealing. HIP pressures range from 50-300 MPa. The high temperature reduces the energy needed to break chemical bonds in the lattice and the isostatic pressure ensures uniform densification.

2.4 Summary

Tungsten and tungsten alloy material systems offer many beneficial properties for extreme environments. While tungsten and tungsten rhenium alloy metallurgy is well understood, AM tungsten alloys are in their infancy. Many of the beneficial properties of tungsten, such as the high melting temperature, are a factor in the difficulty of manufacturing, both traditionally and additively. Traditionally manufactured tung-

sten rhenium parts are limited due to the cost of rhenium. Pure tungsten AM parts are limited to applications such as medical imaging collimators, where limitations of part density are outweighed by the benefits in creating complex, radiation-shielded geometries. The AM tungsten alloy space is largely unexplored, but offers benefits when printing high surface area parts, where the raw material cost is much cheaper than the bulk parts to be subtractively machined.

III. Tungsten Rhenium Study

3.1 Methodology

3.1.1 Overview

In this study, tungsten rhenium alloys prints were made to evaluate the effects of alloy composition, print parameters, and post-print heat treatments on the quality of the part as compared to traditionally manufactured tungsten and tungsten rhenium material properties. The AM parts were compared to bulk tungsten and tungsten rhenium on the basis of cracking, density, and tensile strength. Rhenium is well known to ductilize tungsten [6] and has traditional uses in the welding of tungsten [18], so rhenium was hypothesized to improve print quality due to the similarity of SLM printing to welding, albeit at a much smaller scale. Rhenium was added at 5 and 25 wt% to understand its effect in small and large amounts approaching its solubility limit in tungsten.

Spherical powders for additive manufacturing are expensive, especially unique formulations including large wt% of rhenium. In light of this, the study utilized mixtures of pure elemental powders. The powders were mixed in 100 gram increments in a FlackTek, Inc Dual Asymmetric Centrifuge Speed Mixer at 1600 rpm for 2 minutes. Occasional samples of powder were taken and imaged by SEM during various mixing trials to verify satisfactory mixing was occurring in the different compositions tested. Good mixing was assumed for all other alloy compositions following the same procedure; Figure 6 shows a sample image of the W5Re mixed powder. Pure tungsten powder with an average diameter of 17μm was ordered from Tekna Advanced Materials based in Québec, Canada at a cost of approximately $220 per kg. Mesh-filtered rhenium powder to mix for alloying was provided by Rhenium Alloys at a cost of approximately $3,000 per kg. The spherical nature of the majority powder

(tungsten) facilitated good spreading and packing in the build chamber.

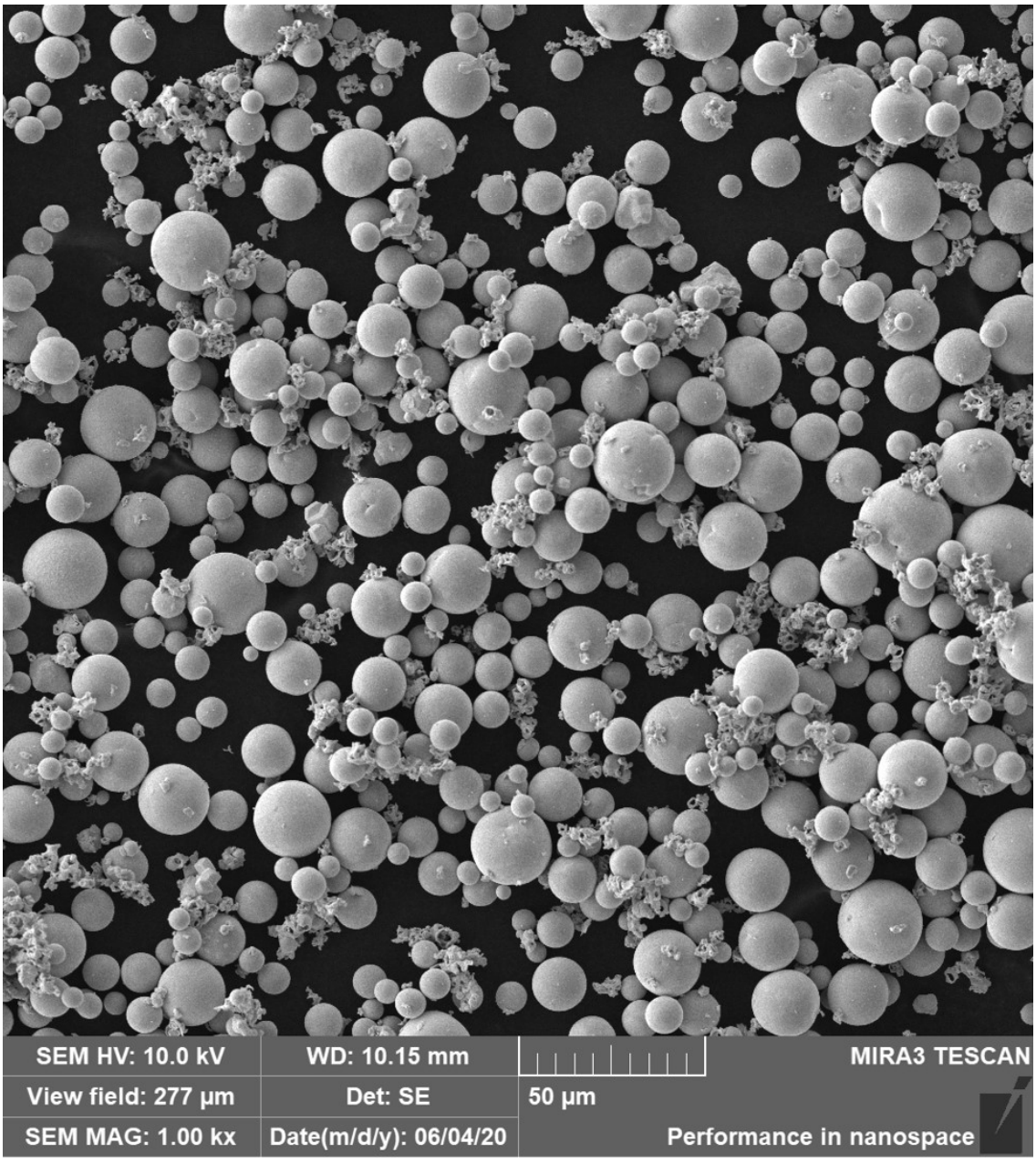

Figure 6. Even mixing observed between spherical W powder produced by plasma atomization and mesh-filtered, mechanically processed granular Re powder

The majority of prints were done on an Mlab 200R Cusing with an argon build chamber (oxygen content 0-0.02%) environment on a steel build plate. All specimens were printed with a layer height of 15 μm. Prints were typically removed by wire

EDM; occasionally prints were brittle enough with such low build plate adhesion they could be removed by hand. Density measurements were made on printed specimens by the Archimedes method in accordance with ASTM B962 [44]. Prior to density measurements, specimen sides were ground on SiC paper to remove roughness, which influences the accuracy of density measurements. After grinding, each specimen was placed in an oven at 120 deg C for one hour to bake out moisture.

3.1.2 Rhenium Percentage

A set of 10mm sided cubes were printed with compositions of W5Re and W25Re with a hatch spacing of 50 μm and laser speeds varying from 100 to 400 mm/s based on previous research in pure tungsten [2]. The cubes were placed in a conductive carbon thermoset puck, ground down to a flat surface, and polished according to the sample procedure in Appendix A. The specimens were then imaged by SEM to analyze cracking. Based on the reduced cracking in the W25Re samples, this alloy was chosen as the focus of continued research. More information on this can be found in the results section of this chapter.

3.1.3 Printing Parameter Selection

After downselecting to the W25Re alloy, 10mm cubes were printed at various laser powers, hatch spacing, and laser speeds to determine the effect of printing parameters on material quality. Laser powers were 100 W, 150 W, or 200 W. Hatch spacings were 25 μm, 50 μm, 75 μm, and laser speeds were 400, 600, 800 and 1000 mm/s. Layer height was set at 15 microns. The cubes were placed in a conductive carbon thermoset puck, ground down to a flat surface, and polished according to the sample procedure in Appendix A. The specimens were then imaged by SEM. All WRe binary alloys printed seemed to exhibit some cracking and density less than 100% of the theoretical

density. More information on this can be found in the results section of this chapter. Two heat treatments were attempted to mitigate the cracking and density issues.

3.1.4 Heat Treatment Post-Processing

Prior to the heat treatments, a set of six miniature tensile bars was printed at 200 W, 50 μm hatch spacing, and 1000 mm/s speed. Three bars were sent to Rhenium Alloys, Inc in Cleveland OH for a hydrogen annealing process. The tensile specimens were placed in a 100% hydrogen environment at 2400 deg C and ambient pressure for 12 hours. The other three tensile specimens underwent Hot Isostatic Pressing (HIP) treatment at American Isostatic Presses, Columbus OH. This was accomplished in a 100% argon environment at 2000 deg C and 30,000 psi for four hours. After the blocks of material and tensile bars finished heat treatment, they were prepared for metallographic analysis by the technique discussed in Appendix A. Tensile testing of the heat treated and non-treated material is discussed in Section 3.1.6.

3.1.5 Build Plate Material Study

During the study, many prints would fail at small build heights of less than 2 mm, causing the remaining print layers to fail. Failure would proceed by poor bonding of molten powder to the previous layer and liftoff by thermal deformation. Even in successful prints, slight lifting or curling would occur at the edges of the printed parts and the stainless steel build plate commonly used in the Mlab AM machine. It was hypothesized that the mismatch of thermophysical properties between steel and the tungsten alloy laser welds was leading to the poor bond between the materials. A small build plate study was conducted using the supplied stainless steel print surfaces, as well as individual print surfaces inlaid into a specially fabricated build plate. This build plate allowed for up to five different metal pucks to be inset with the build

surfaces for multiple trials. Prints were then constructed using 50 μm hatch spacing, 200 W laser power, and various speeds to optimize print quality. Pucks of the following materials were examined: stainless steel, copper, titanium, and tungsten. Select material properties of the materials chosen are shown below in Table 2.

Material	**Melting Point (K)**	**Density (g/cm3)**	**Thermal Conductivity W/(m K)**	**Thermal Diffusivity mm2/s**	**Solubility in Tungsten**
Copper	1357	8.96	401	119	None
Stainless Steel 304	1450	7.9	16.3	4	Extensive
Tungsten	3695	19.246	173	67	Unlimited
Titanium	1941	4.506	21.9	9	Extensive

Table 2. Selected material properties of the build plate materials used.

Tungsten was chosen because of its similarity to the printed materials, copper for similarity in thermophysical properties and low cost, titanium because of its similarity to steel in thermophysical properties but having some solubility with tungsten, and stainless steel as a baseline. Figure 7 shows a picture of WReHfC prints on pucks made from 100% copper (Cu).

Figure 7. Four Cu individual print surface pucks with various WReHfC prints

W25Re was then printed in 2 mm tall, 10 mm diameter cylinders at laser speeds

between 400 mm/s and 1000 mm/s. The metal build plate pucks were sectioned in half and examined using optical microscopy to observe build plate interaction. The primary areas of investigation were the quality of the bond between the built material and the substrate as well as the cracking in the printed material near the build plate. The transition region was examined at the outer edges of the cylinder which was usually lifted, as well as the center which was usually well-adhered.

3.1.6 Tensile Testing

During the initial parameter study, quality of the printed surfaces was shown to be greatly reduced at powers lower than 200 W. Hatch spacing of either 25, 50, or 75 μm m and various laser speeds had a less obvious effect, thus these parameters were varied for the tensile test specimens while power was kept constant at 200 W. The tensile test specimens were based off of ASTM E8 [45] specimens. However, the smallest subsize specimens in ASTM E8 were still too large to fit a reasonably large set in the build chamber. Therefore miniature tensile bars were designed with 83 mm length rather than the subsize 100 mm. The other dimensions were scaled accordingly, with a neckdown radius consistent with the standard. The miniature tensile bars were printed in both the vertical and horizontal configuration at laser speeds of 400, 600, 800 and 1000 mm/s. Once removed from the build plate, each tensile bar was placed in an MTS hydraulic tensile test machine and pulled vertically until failure at a displacement rate of 0.0005 mm/s, sufficiently slow to provide a quasistatic loading rate in accordance with ASTM E8 [45]. This was repeated for all speeds, orientations, and heat treated specimens. The specimens were then removed and placed in the SEM to examine the fracture surfaces.

3.2 Results

3.2.1 Rhenium Content

The following figure shows SEM images of the top surfaces of printed tungsten rhenium alloys. The parts were manufactured by a zig-zag welding strategy. Thus, the parts appear to have overlapped weld lines. The primary focus, however, is the quality of the surface topography and cracking. In Figure 8a, pure tungsten struggles to be made completely dense by AM because of balling, oxidation, and voiding. The high DBTT of tungsten causes microcrack networks to form along the brittle material finding the lowest stable energy state. This connects the cracks along the voids and weak grain boundaries due to interstitial oxygen and poorly melted tungsten powder. Figure 8b shows W5Re; note the much-improved surface quality in that voids and balling are less common, however cracking is still present. This suggests weak intergranular bonding causing cracks to again form along the highest dislocation stress regions. Finally, W25Re is show in Figure 8c, the cracking is significantly reduced in addition to the improvements noted with W5Re.

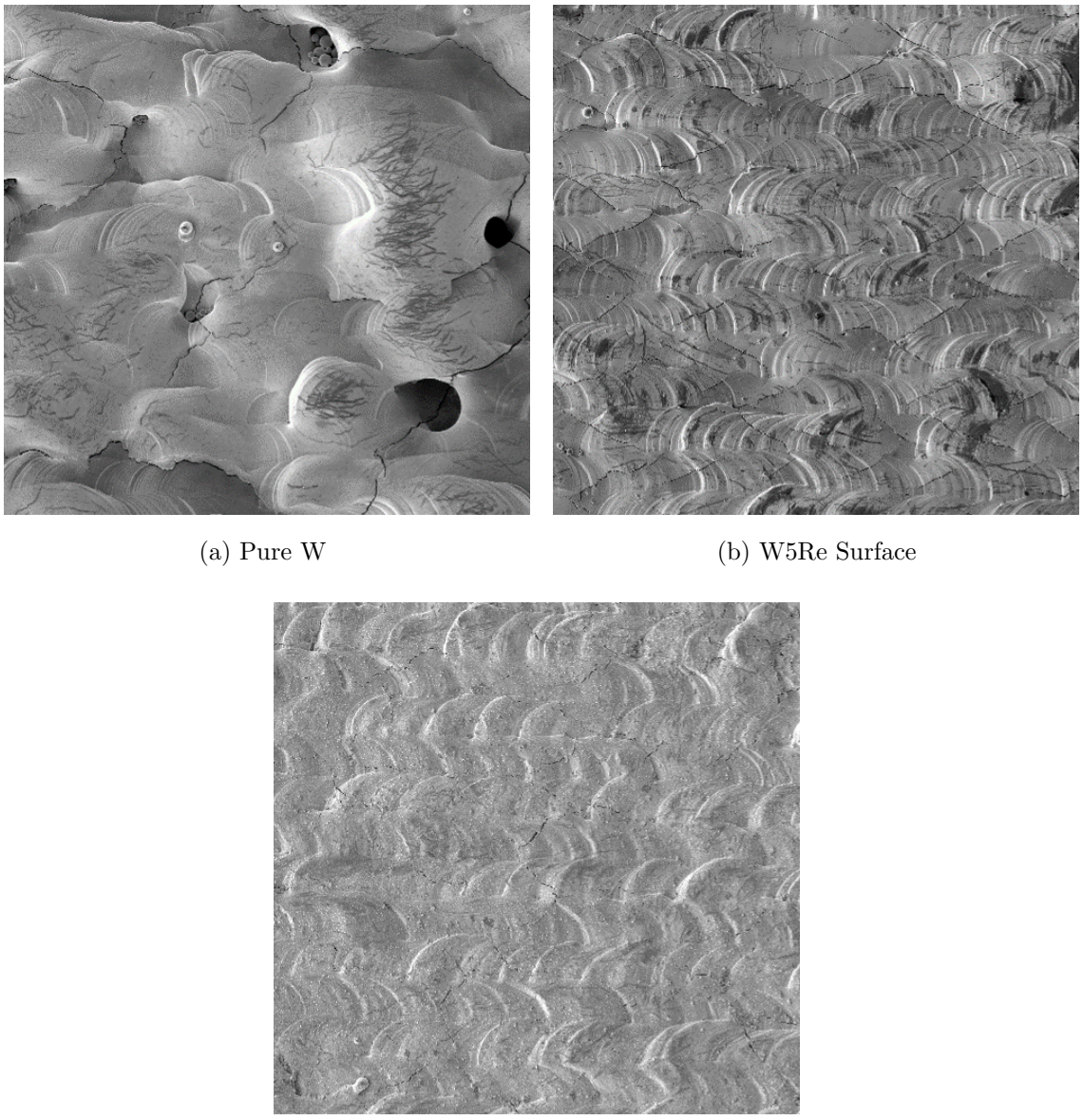

(a) Pure W

(b) W5Re Surface

(c) W25Re Surface

Figure 8. Microcracking in Pure W, W5Re, and W25Re at Optimal Print Parameters200x Zoom

3.2.2 Tensile Testing

This study tested 18 horizontally printed tensile bars, 11 vertically printed tensile bars, 3 hydrogen annealed tensile bars, and 1 post-HIP tensile bar. The heat treated specimens were printed vertically with laser speeds of 1000 mm/s and hatch spacing

of 50μm The horizontally printed bars varied hatch spacing and laser speed. The hatch spacing showed negligible effect on both microcracking and tensile strength. The vertically printed specimens had a constant hatch spacing of 50 μm, but varied laser speed. Table 3 shows the tensile test results for various print parameters of W25Re printed flat against the build plate, while Table 4 shows results for tensile bars printed vertically. High deviation was shown in the ultimate tensile strength (UTS). No significant difference in build direction on UTS was observed, with the caveat that some vertically printed specimens had large cracks in the gauge section leading to instantaneous failure upon initial loading. The average UTS of the horizontally printed specimens was 263 ± 50 MPa, while the average of the vertically printed specimens was 173 ± 160 MPa. The vertically printed specimens had multiple near-immediate failures indicating large pre-existing defects in the specimen. Removing these outliers from the sample gave an average of 321 ± 37 MPa. Figures 9 and 10 show no statistically significant relationships between laser speed, or E_v and the UTS, while Figure 11 shows slight evidence of 50 μm providing improved strength. The effects of heat treatment on UTS are displayed in Figure 12. The results show strong evidence of both heat treatments raising the UTS, with H annealed specimens reaching almost 700 MPa. High variation in UTS was likely due to high variation in the additive manufacturing process, including oxygen content, exact powder chemistry, and randomness in stress relief as the material cooled. Of these effects, oxygen content is likely the most influential. Previous literature of SLM printed tungsten and tungsten tantalum alloys showed higher densities in parts manufactured with less oxygen [41]. The MLab 200R used in this study had a resolution of approximately 1000 ppm of oxygen, thus, variations in oxygen levels would be undetectable during printing.

Hatch Spacing (μm)	Speed (mm/s)	Ev (W/mm^3)	Gauge Width (mm)	Gauge Thick (mm)	Max Force (N)	Stress (MPa)
75.00	200.00	888.89	3.26	5.79	4555.49	241.35
75.00	200.00	888.89	3.27	5.79	4388.03	231.96
75.00	200.00	888.89	3.32	5.76	3756.79	196.45
75.00	1000.00	177.78	3.20	5.76	4825.87	262.46
75.00	1000.00	177.78	3.22	5.78	3803.16	204.34
75.00	1000.00	177.78	3.21	5.71	4715.78	257.28
75.00	800.00	222.22	3.23	5.94	5332.90	277.95
75.00	800.00	222.22	3.21	5.93	5302.80	278.58
75.00	800.00	222.22	3.22	5.92	5393.80	282.95
75.00	400.00	444.44	3.25	5.87	7728.32	405.10
75.00	400.00	444.44	3.30	5.85	4429.11	229.43
75.00	400.00	444.44	3.23	5.83	4845.18	257.30
50.00	1000.00	266.67	3.23	2.95	3263.70	342.52
50.00	800.00	333.33	3.25	2.97	2854.00	295.67
50.00	600.00	444.44	3.28	2.96	2317.80	238.73
75.00	600.00	296.30	3.26	3.00	2066.00	211.25
25.00	800.00	666.67	3.25	2.99	2389.00	245.85
25.00	1000.00	533.33	3.22	2.98	2589.00	269.81

Table 3. Printing Parameter Tensile Test Data for Horizontally As-Printed Specimens

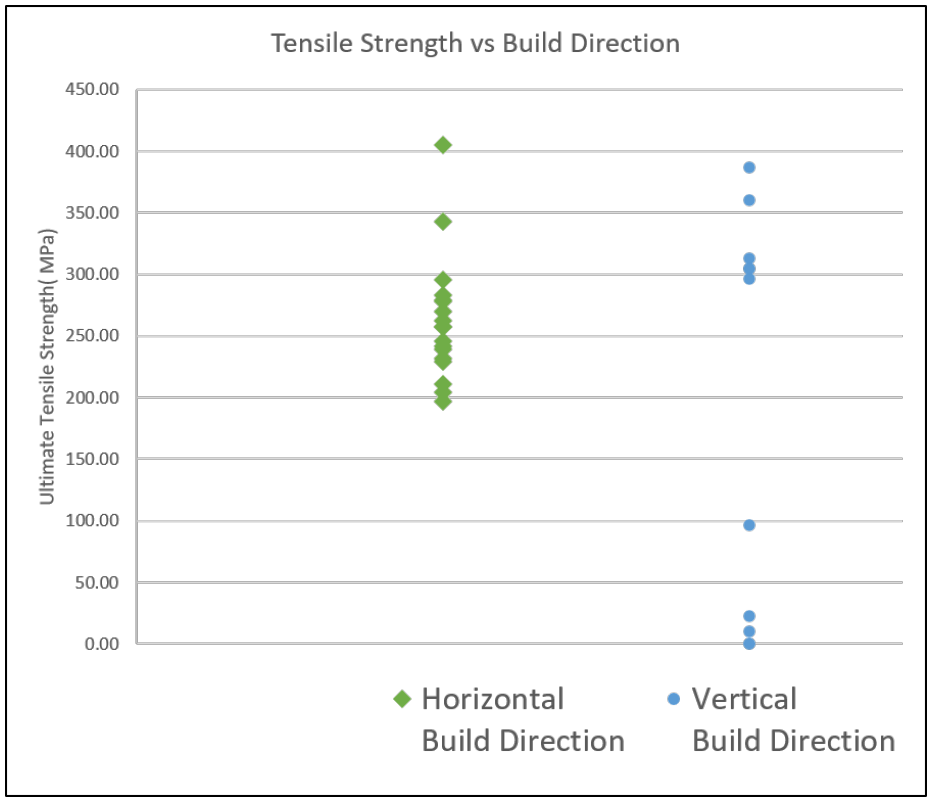

Figure 9. UTS vs Build Direction of Tensile Bars

Hatch Spacing (μm)	Speed (mm/s)	Ev (W/mm^3)	Gauge Width (mm)	Gauge Thick (mm)	Max Force (N)	Stress (MPa)
50	400	667	2.92	2.89	0	0
50	400	667	2.77	2.76	2328	304.5048
50	400	667	2.92	2.89	2574	305.0197
50	700	381	2.87	2.83	0	0
50	700	381	2.84	2.88	2947	360.3042
50	700	381	2.87	2.84	3149	386.3424
50	1000	267	2.78	2.85	84	10.60204
50	1000	267	2.79	2.85	178	22.38571
50	1000	267	2.78	2.86	768	96.59405
50	1000	267	2.74	2.58	2096	296.4975
50	1000	267	2.79	2.85	2487	312.7712

Table 4. Printing Parameter Tensile Test Data for Vertically As-Printed Specimens

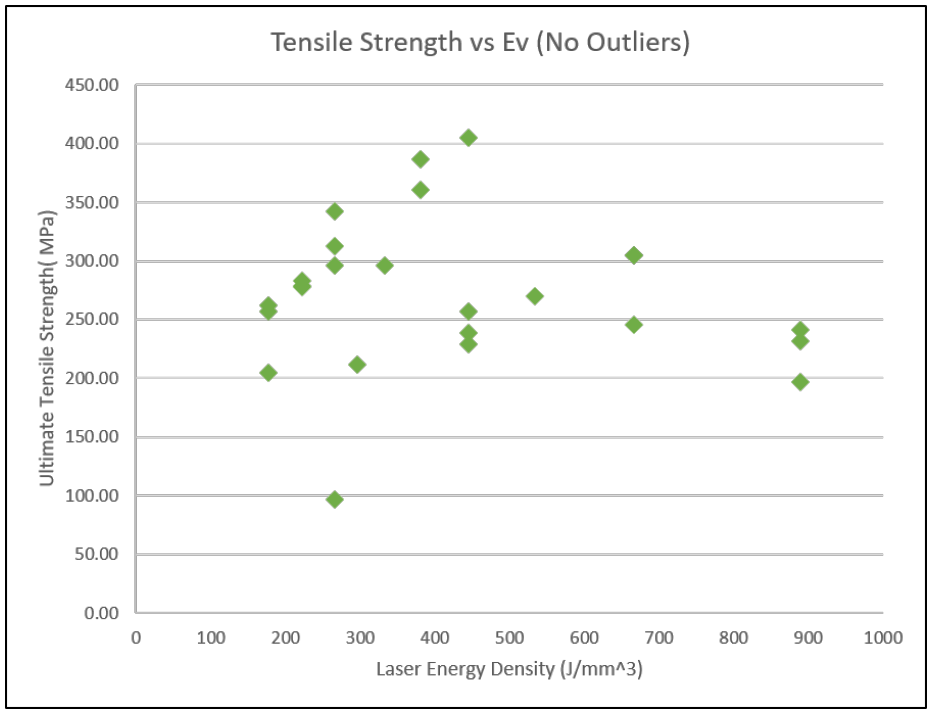

Figure 10. UTS vs E_v

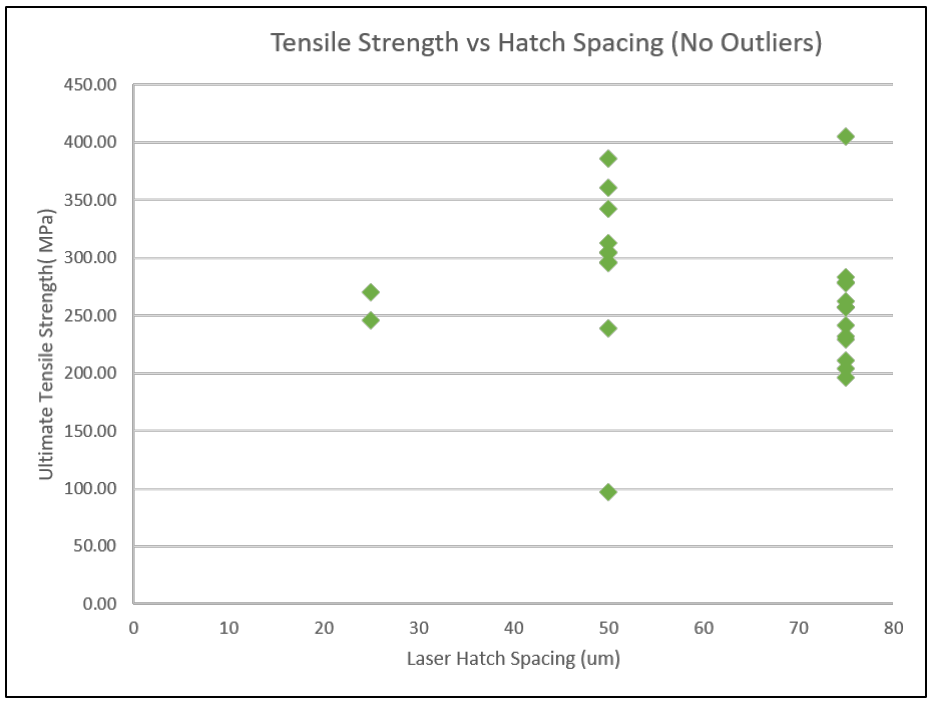

Figure 11. UTS vs Hatch Spacing

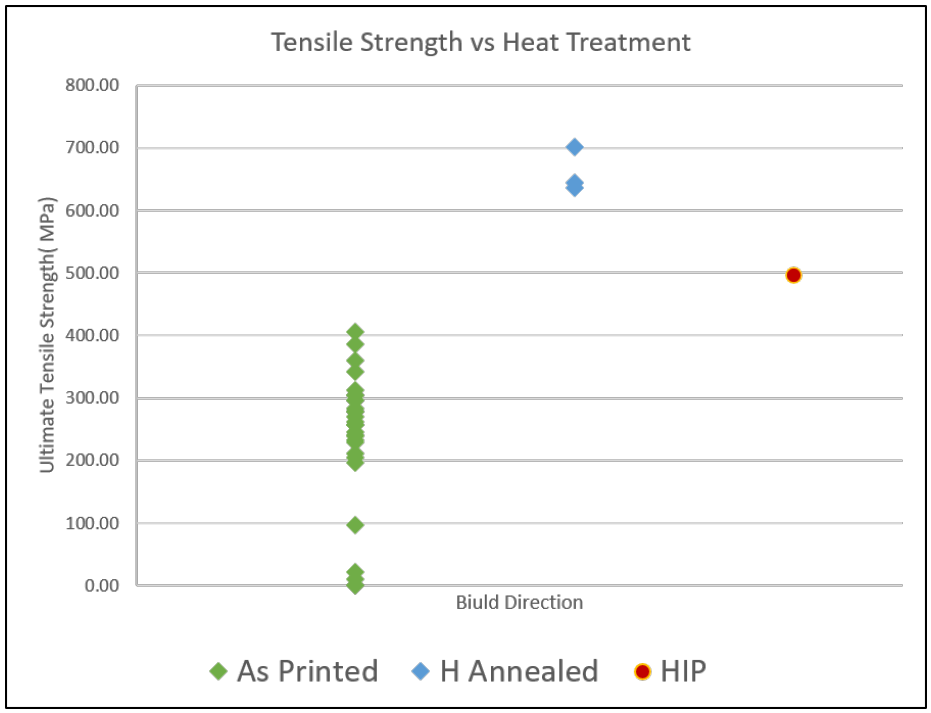

Figure 12. UTS vs Post-Print Heat Treatments

Figures 13 through 16 show the fracture surfaces of tensile specimens manufac-

tured with process parameters of 50 μm m hatch spacing, 200 W laser power, and various laser speeds. Figures 17 and 18 show fracture surfaces of specimens printed at 50 μm m hatch spacing, 200 W laser power which underwent HIP and H Annealing, respectively.

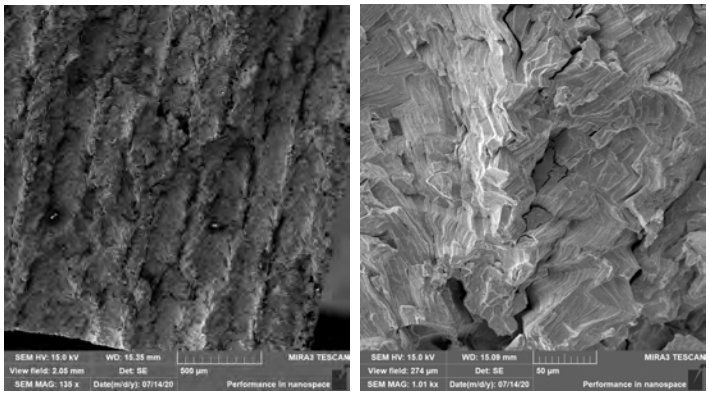

(a) Surface at 135x (b) Surface at 1000x

Figure 13. Fracture Surface of Print with 200 mm/s Laser Speed

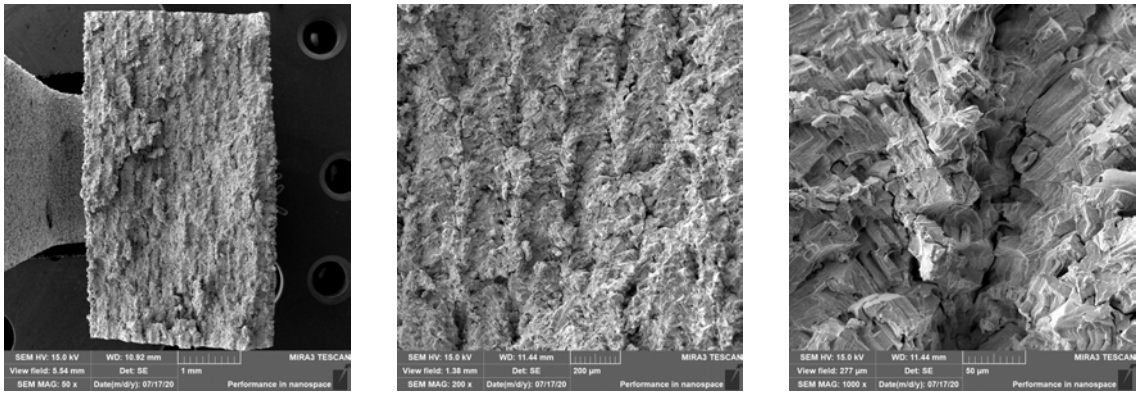

(a) Surface at 50x (b) Surface at 200x (c) Surface at 1000x

Figure 14. Fracture Surface of Print with 400 mm/s Laser Speed

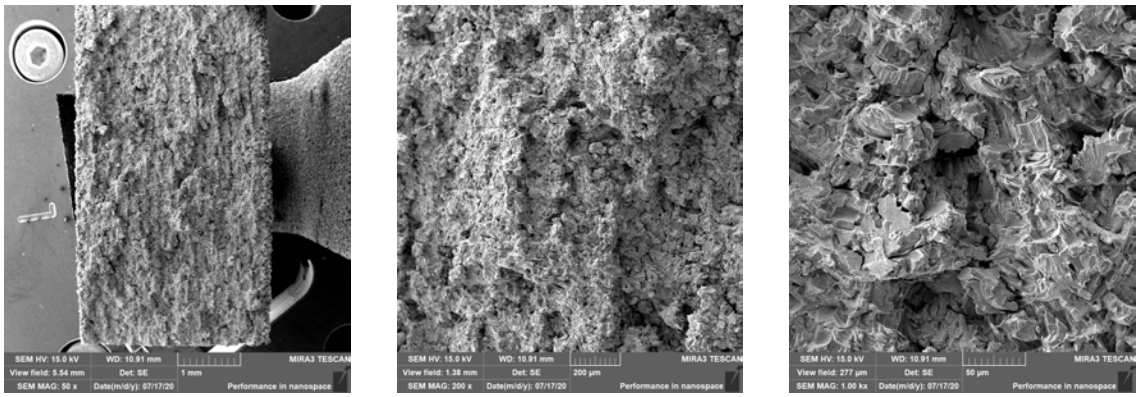

(a) Surface at 50x (b) Surface at 200x (c) Surface at 1000x

Figure 15. Fracture Surface of Print with 800 mm/s Laser Speed

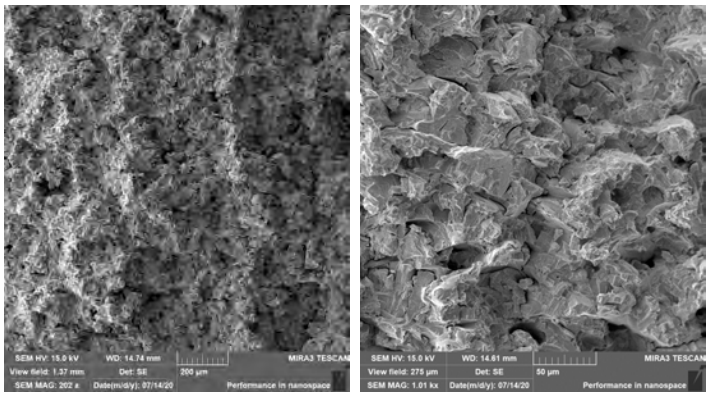

(a) Surface at 200x (b) Surface at 1000x

Figure 16. Fracture Surface of Print with 1000 mm/s Laser Speed

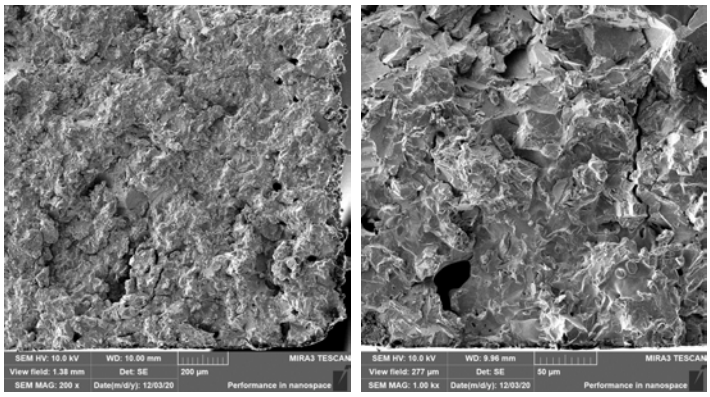

(a) Surface at 200x (b) Surface at 1000x

Figure 17. Fracture Surface of Post-HIP Parts Printed at 1000 mm/s Laser Speed

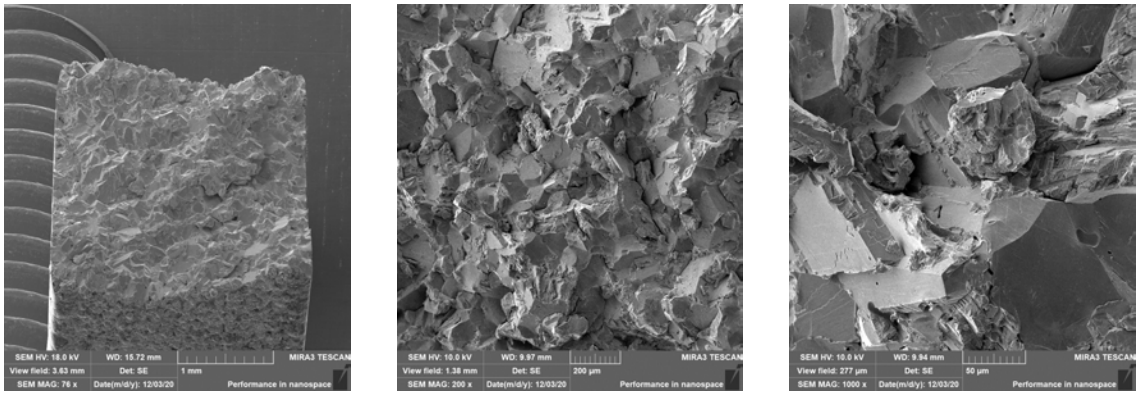

(a) Surface at 76x (b) Surface at 200x (c) Surface at 1000x

Figure 18. Fracture Surface of Hydrogen Annealed Parts Printed at 1000 mm/s Laser Speed

3.2.3 Build Plate Material Study

In order of best (fewest failed prints) to worst (most failed prints) the print surfaces were:

1. Copper
2. Stainless Steel
3. Titanium

4. Tungsten

Copper build surfaces showed significant improvement over all other print surfaces when printing W25Re parts on all laser speeds (400 - 1000 mm/s). A stainless steel surface produced mostly successful prints at 1000 mm/s laser speed, however, slower speeds producing better reduction in microcracking also failed more often as speed was lowered. Titanium build surfaces would occasionally produce successful parts at higher laser speeds (800-1000 mm/s), however, both stainless steel and titanium had weak bonds between the build plate and the printed part. Printing on pure Tungsten pucks proved infeasible at any speed. Figures 19 - 24 show optical microscope images taken of pucks printed with various laser speed settings sectioned through the center of the W25Re printed cylinder.

(a) 400 mm/s

(b) 1000 mm/s

Figure 19. Copper build plate half-section. Strong adhesion shown at all print speeds.

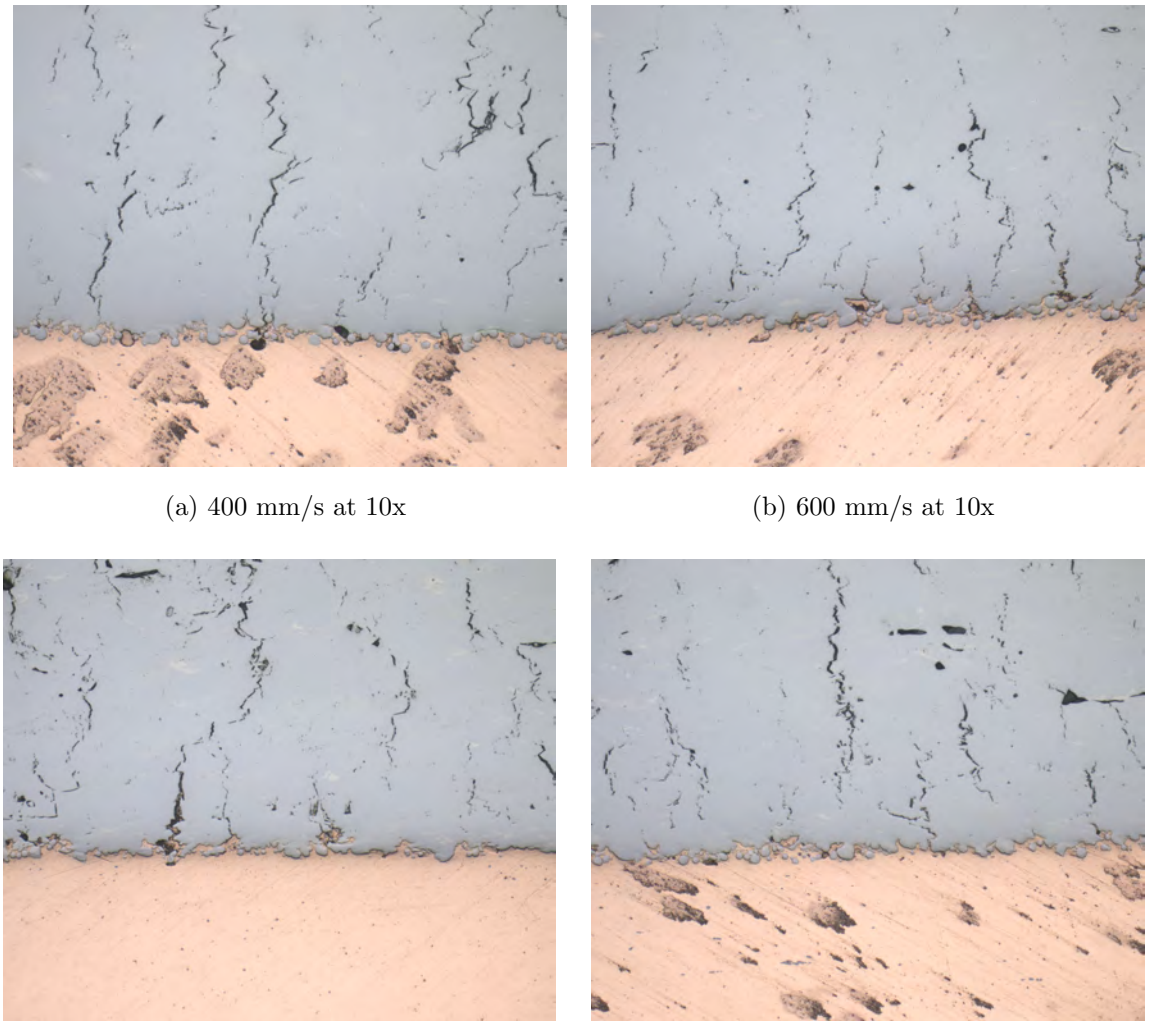

(a) 400 mm/s at 10x

(b) 600 mm/s at 10x

(c) 800 mm/s at 10x

(d) 1000 mm/s at 10x

Figure 20. Copper build plate interactions at the center of the print. The discolorations in the copper are surface finish imperfections from the polishing process and are not relevant.

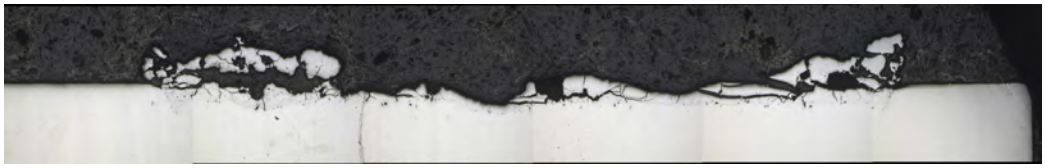

(a) 400 mm/s

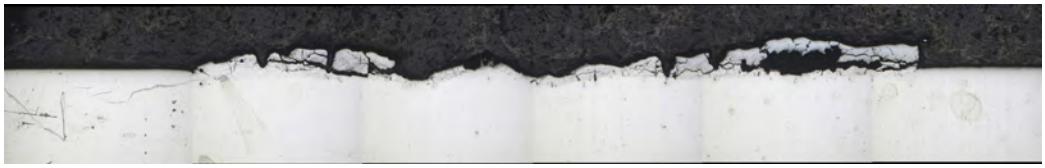

(b) 600 mm/s

(c) 800 mm/s

(d) 1000 mm/s

Figure 21. Stainless Steel build plate half-section. Good adhesion shown at higher print speeds.

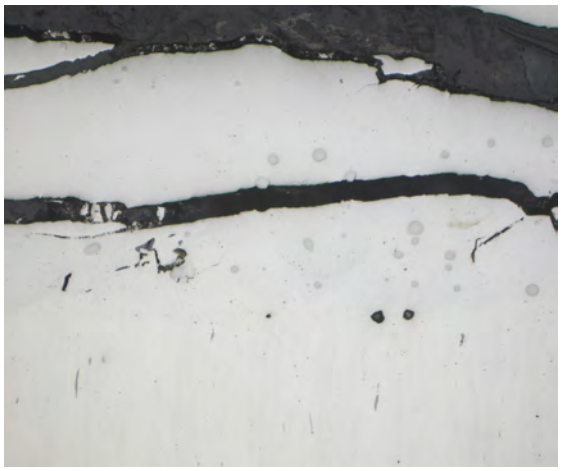

(a) 400 mm/s at 20x

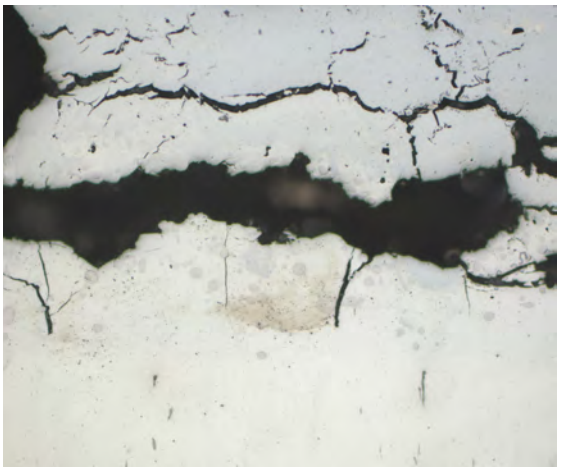

(b) 600 mm/s at 20x

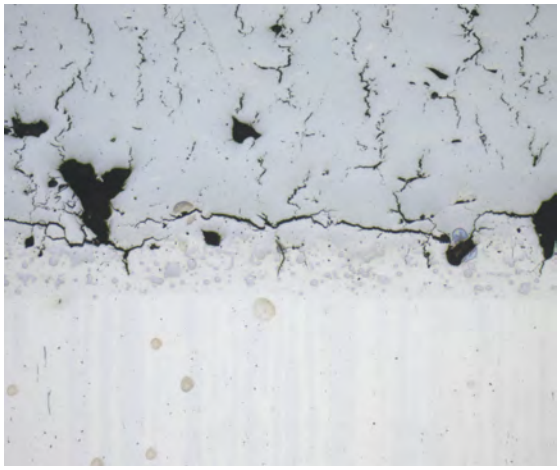

(c) 800 mm/s at 10x

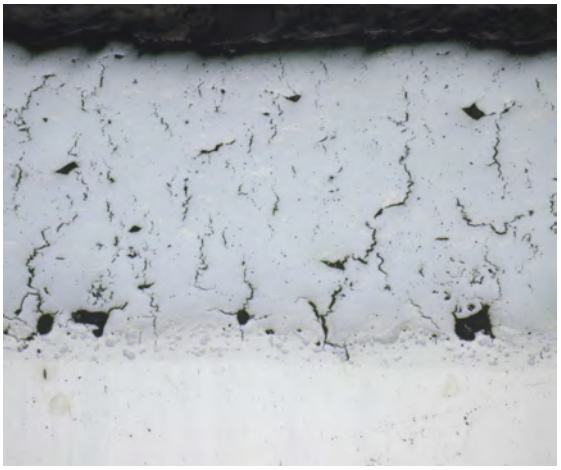

(d) 1000 mm/s at 10x

Figure 22. Stainless Steel Build Plate Interactions

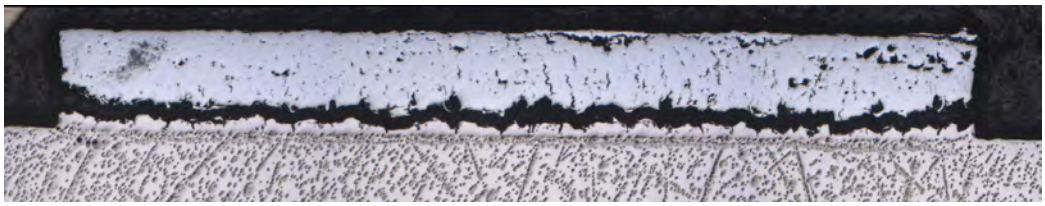

(a) 600 mm/s

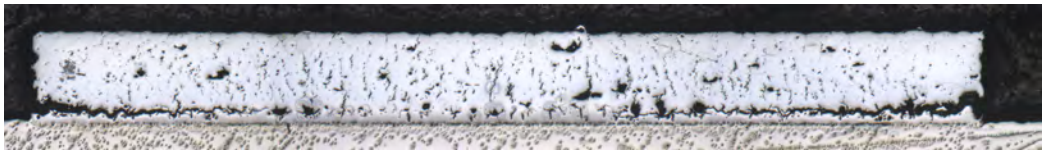

(b) 800 mm/s

(c) 1000 mm/s

Figure 23. Titanium build plate sections. Study prints failed on slower speeds and exhibit severe horizontal cracking near the build plate on higher speeds, resulting in strong lifting and print failure in taller parts.

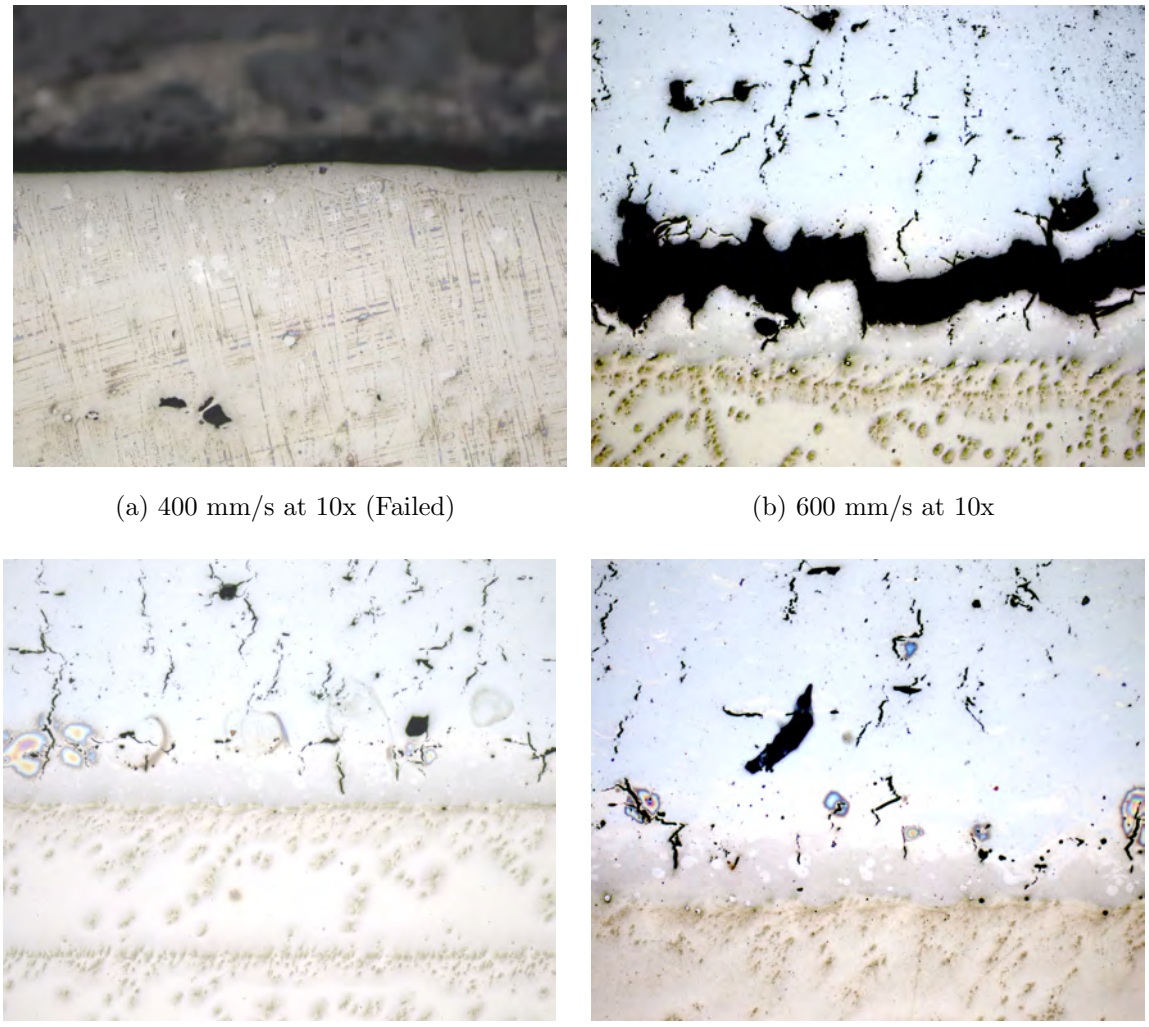

(a) 400 mm/s at 10x (Failed)

(b) 600 mm/s at 10x

(c) 800 mm/s at 10x

(d) 1000 mm/s at 20x

Figure 24. Copper Build Plate Interactions

The likely cause of the strong copper adhesion is its low melting temperature and insolubility with tungsten. The worst performing print surface, a traditionally manufactured pure tungsten puck, would not print at any speed attempted. The print surfaces resulted in a more adhered print the lower the melting temperature. Copper was the only surface tested that was insoluble in tungsten, so there may be compounds forming that result in poor surface adhesion. The tungsten powder's melting point is higher than the copper substrate, which may result in a melted pool

of copper mixed with the tungsten powder at various amounts melted. This likely serves as a mechanical bond similar to hook and loop fabric fasteners. This seems to be supported by the close-up images of the copper build plate bond (Fig 20). Tungsten rhenium alloys are known to assist with friction stir-welding [3].

3.2.4 Cracking

As rhenium content increases from 0 to 5 to 25 wt%, microcracking is reduced but not entirely eliminated. Whereas pure tungsten printed well at laser scan speeds of 100-400 mm/s [2], adding rhenium lowered the combined melting temperature, requiring less energy input. Thus, faster speeds (and therefore lower energy density) of 400-1000 mm/s produced parts with high geometrical fidelity to the original 3D model. See Figures 25 and 26 in Chapter 4.1 for an SEM imagery comparison of all alloy compositions.

3.2.5 Hardness Testing

Samples of produced AM W25Re and W25Re1HfC parts were sent to Miami Valley Materials Testing Center in Tipp City OH for hardness testing. The report summary can be found in Appendix C. Table 5 below shows both the Vickers and Rockwell hardness results for W25Re parts as printed and those which underwent post-postprocessing heat treatments. Both HIP and H annealing show little effect on the hardness of the printed parts.

Sample	Composition and Treatment	Avg Vickers (with 500-gram load)	Avg Rockwell C Hardness Scale
1	W25Re As Printed	430.4	43.6
2	W25Re As Printed	448.9	45.2
3	W25Re HIP	454.7	45.7
4	W25Re HIP	442.5	44..7
5	W25Re H Annealed	430.4	43.6
6	W25Re H Annealed	451.9	45.4

Table 5. Vickers Hardness Scale with a 500 gram load and Rockwell C Hardness Scale results for different compositions and heat treatments of AM W alloy parts

3.3 Summary

AM tungsten alloyed with rhenium greatly reduces cracking and allows for tensile testing rather than immediate failure. In addition, laser hatch spacing of 50 μm was slightly better than 25 or 75 μm while power was optimal at 200 W. Optimal laser scan speed depended on the amount of rhenium in the alloy composition, but produced geometrically faithful parts at laser scan speeds between 400 and 1000 mm/s with the lowest microcracking at the lowest scan speed. The provided stainless steel build plate produced prints most of the time, especially with a laser scan speed of 1000 mm/s. The copper build surface was able to consistently produce W25Re parts at any laser

scan speed between 400 and 1000 mm/s. The tensile tests had high variability in the as-printed part UTS with little influence from print parameters. The heat treated W25Re specimens both outperformed the as-printed specimens, with the hydrogen annealed alloy reaching almost 100% of traditionally manufactured UTS.

IV. Tungsten Rhenium Hafnium Carbide Study

4.1 Methodology

4.1.1 Overview

In this study, WReHfC alloys were manufactured and downselected based on optimal compositions and print settings based on density values, SEM images, and EBSD maps.

4.1.2 Rhenium and Hafnium Carbide Percentages

A set of 1mm tall, 10mm diameter cylinders were printed at various levels of tungsten, rhenium, and hafnium carbide percentage content by weight. Table 6 below lists the alloy parameter space:

% Tungsten	% Rhenium	% Hafnium Carbide
99	0	1
98	0	2
96	0	4
94	5	1
93	5	2
91	5	4
74.5	25	0.5
74	25	1
73	25	2
71	25	4

Table 6. W, Re, HfC Alloy Composition Percentage By Weight

These cylinders were placed in a conductive carbon thermoset puck, ground down to a flat surface, and polished. The pucks were imaged with the SEM to examine surface and weld track quality.

4.1.3 Printing Parameter Selection

Keeping a consistent power of 200 W and hatch spacing of 50 μm based on the previous W25Re study, 10mm diameter cylinders were printed at various laser speeds on Cu print surface pucks. Attempts using any other surface were unsuccessful due to high print lifting causing print failure. Laser speeds were 400, 600, 800 and 1000 mm/s. The cylinders were placed in a conductive carbon thermoset puck, ground down to a flat surface, and polished. The pucks were placed in the SEM to be imaged. Laser scanning strategies tested including the standard zig-zag, a 4mm square checkerboard strategy, and a skin-core strategy were attempted without noticeable effect.

4.1.4 Tensile Testing

Keeping a consistent power of 200 W and hatch spacing of 50 μm based on the previous W25Re study, laser energy density, E_v, was varied by laser speed. However, only one W25Re1Hfc tensile bar was able to be manufactured at any speed. This was only accomplished by constructing a raft of W25Re on a stainless steel build plate, stopping the build mid-print when over 1mm build height was achieved, emptying the powder chamber and refilling it with a W25Re1Hfc powder composition. Three tensile bars were printed in this manner, however two fractured during EDM machining to remove the specimens from the raft and plate.

4.2 Results

4.2.1 Hafnium Carbide Content

Figures 25 and 26 are a collage of SEM imaging with varying rhenium and hafnium carbide content. All imaged specimens were printed at 50 micron hatch spacing and

a laser power of 200 W. Figure 25 shows SEM images of prints with laser speeds of 400* mm/s and Figure 26 shows prints at laser speeds of 1000* mm/s.

*NOTE: The exceptions to these are the pure W and W5Re prints. In the set of 400 mm/s images, the W and W5Re printed with laser speeds of 100 mm/s. In the set of 1000 mm/s laser speed images, they printed at a speed of 400 mm/s. This is for two reasons: first, the pure W and W5Re work was done prior to all other work. Second, the low rhenium and hafnium carbide content in each meant the melting temperature of the more pure W powder was raised. Thus the 100 and 400 mm/s correspond to a "slow" and "fast" printable speed analogous to the 400 and 1000 mm/s slow/fast speeds of the higher rhenium and hafnium carbide alloys.

In general, less laser melting occurred as the HfC content increased in pure W, W5Re, and W25Re samples. This was evidenced by irregular circular shapes in the SEM images along with an increased number of voids. These circular shapes are regions of poorly melted powder. Higher laser speeds corresponding to less energy input into the powder layer show similar SEM results to higher HfC content at slower speeds. All surfaces showed evidence of microcracks except for the W25Re1HfC composition at 400 mm/s.

4.2.2 Build Plate Material Study

The only material able to successfully and consistently print W25Re1HfC was copper. Even on copper, print edges showed lifting after approximately 0.25 mm of print height. A set of three W25Re1HfC tensile bar specimens was also successfully printed using a raft of W25Re, but this strategy is time consuming as well as tenuous: two of the three specimens broke during wire EDM removal from the raft/plate.

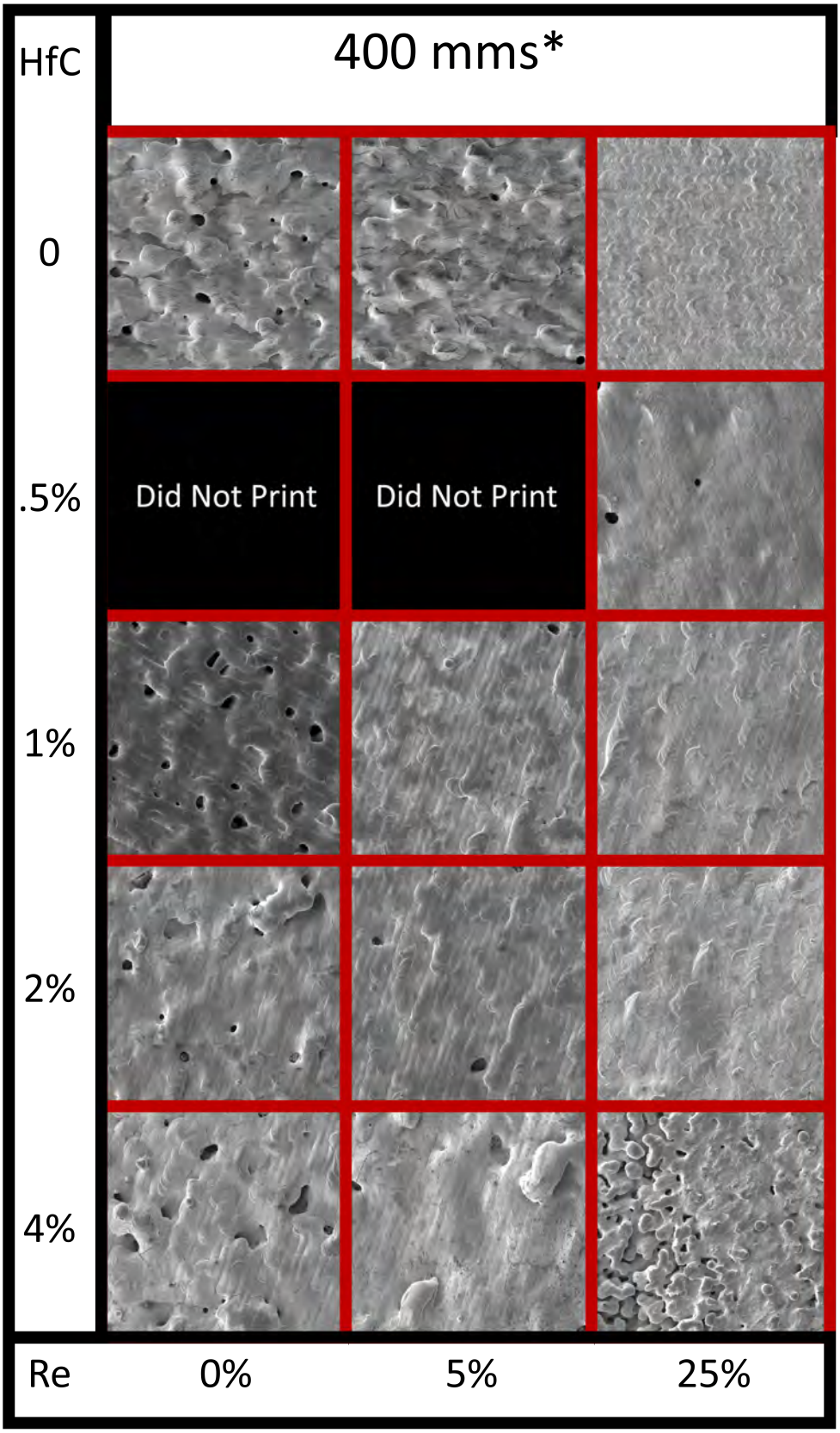

Figure 25. SEM images at 200x of varying amounts of Re and HfC alloys in W at 400* mm/s laser speeds

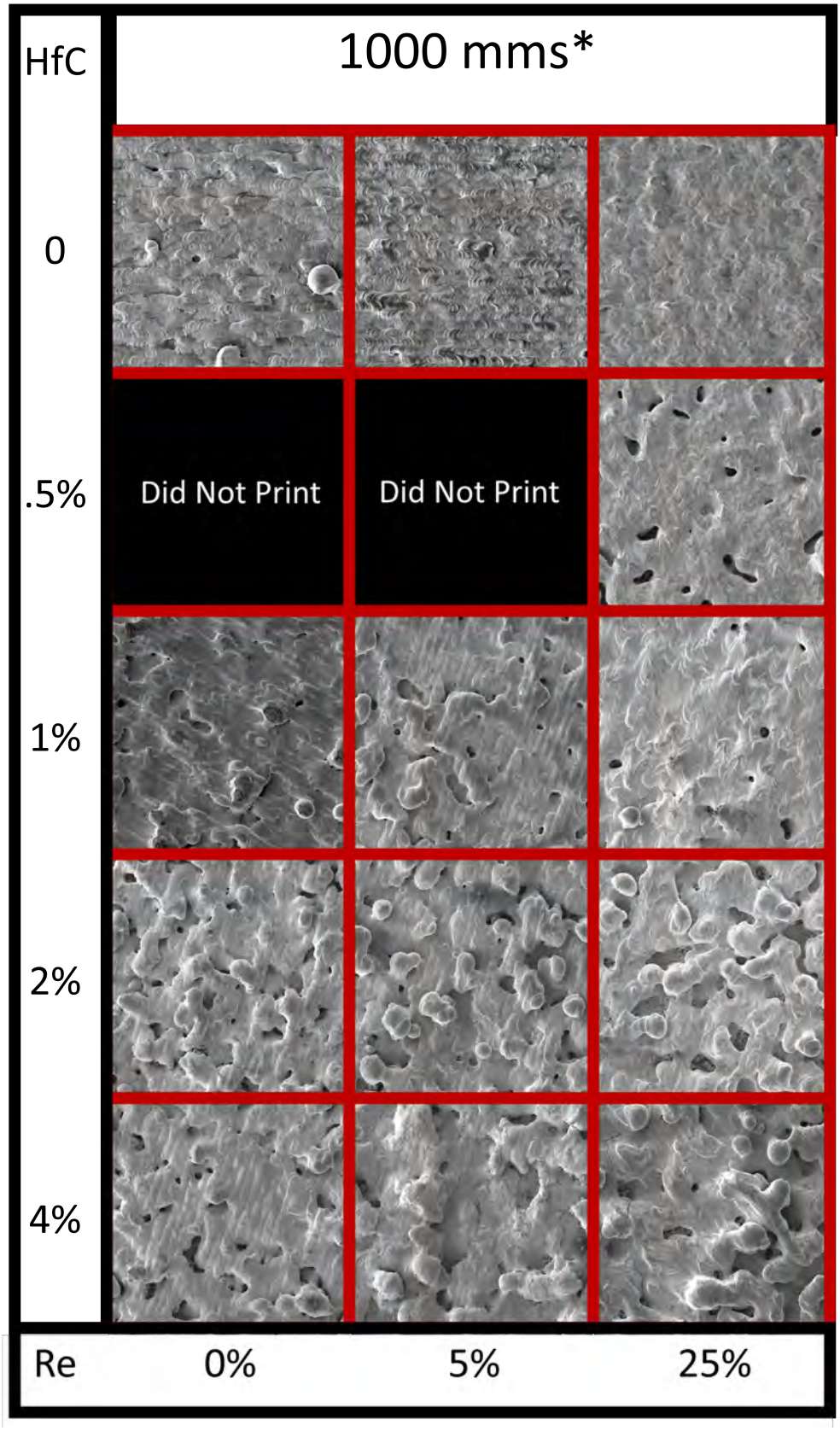

Figure 26. SEM images at 200x of varying amounts of Re and HfC alloys in W at 1000* mm/s laser speeds

4.2.3 Cracking in As-Printed Parts

Microcracking was eliminated in W25Re1HfC printed parts. However, large thermal gradients produced lifted print edges as stated before, along with visible macro cracking primarily along horizontal build layers. This lifting occurred in the first 0.25 mm of the print height, and none of the scan strategies with or without rafts had an effect on lifting.

4.2.4 Hardness Testing

Table 5 was reproduced below as Table 7 to include the hardness results of the W25Re1HfC alloy composition. The HfC alloy was approximately 150 HV_{500} higher than any of the W25Re samples.

Sample	Composition and Treatment	Avg Vickers (with 500-gram load)	Avg Rockwell C Hardness Scale
1	W25Re As Printed	430.4	43.6
2	W25Re As Printed	448.9	45.2
3	W25Re HIP	454.7	45.7
4	W25Re HIP	442.5	44..7
5	W25Re H Annealed	430.4	43.6
6	W25Re H Annealed	451.9	45.4
7	W25Re1HfC As Printed	605.0	55.5
8	W25Re1HfC As Printed	584.9	54.4

Table 7. Vickers Hardness Scale with a 500 gram load and Rockwell C Hardness Scale results for different compositions and heat treatments of AM W alloy parts

4.2.5 Tensile Testing

Due to only one sample surviving wire EDM removal from the build plate and raft, only one tensile test was performed. The result was failure at 132 MPa. This is much lower than all other results except for the immediate failures of the W25Re prints with visible cracking in the gauge section that failed almost immediately. It is

possible that this is an outlier, but cannot be known for sure without more specimens to test. However, several factors point to this being close to the correct value. The hardness test results show the W25Re1HfC prints are much harder than the other compositions. This would lead to the conclusion they would be more brittle as a result. In addition, the lower amounts of microcracking in the material likely led to high amounts of residual thermal stresses as the print cooled. This accounts for both the print edge lifting as well as the high amounts of visible cracks in the printed parts. A few large starting crack-tips would lead to a lower UTS in otherwise microcrack-free parts of high density.

4.3 Summary

W25Re1HfC produced by AM machines is a hard and brittle, yet dense and microcrack-free material.

V. Observations and Analysis

5.1 Overall Effects

The AM parts were evaluated quantitatively by density and tensile strength, and qualitatively by SEM imaging. Table 8 shows each selected print composition average density and tensile strength.

Material / Post-Process	Avg. Density (% Theoretical)	Ultimate Tensile Strength (MPa)
W As Printed	93.00	N/A (Immediate Failure)
W25Re As Printed Horizontal	96.01	262 ± 50
W25Re As Printed Vertical		321 ± 37 (of sample above 100) 26 ± 40 (of sample below 100) 173 ± 160 (entire sample)
W25Re HIP	96.68	496
W25Re H Anneal	98.17	660 ± 36
W25Re1HfC As Printed	97.00	132

Table 8. Final Downselected Materials with Average Densities and UTS

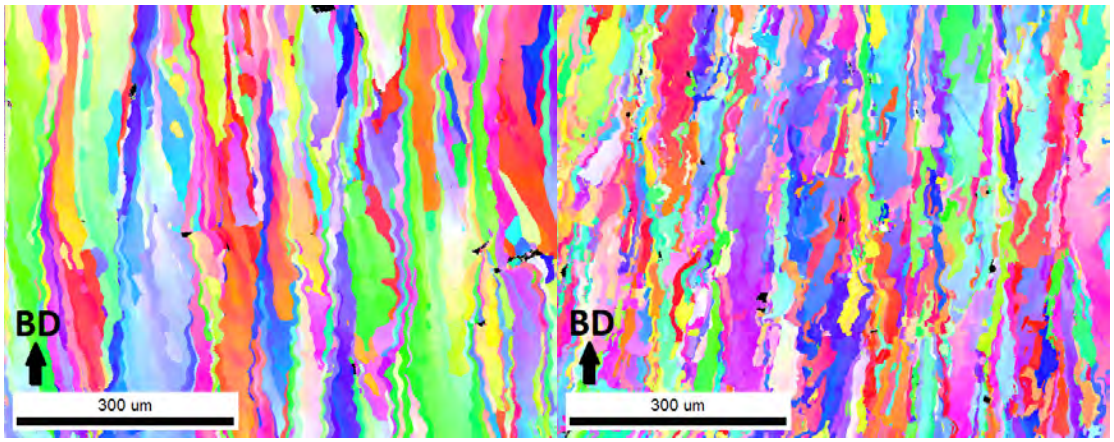

(a) Pure W, avg size: 30 x 352 μm (b) W5Re, avg size: 14 x 166 μm

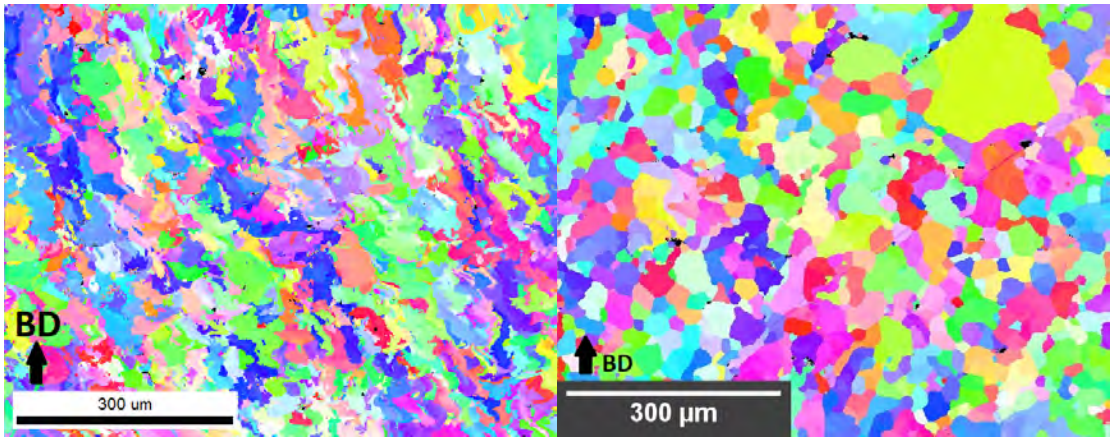

(c) W25Re As Printed, avg size: 13 x 73 μm (d) W25Re Post-HIP, avg diameter: 33 μm

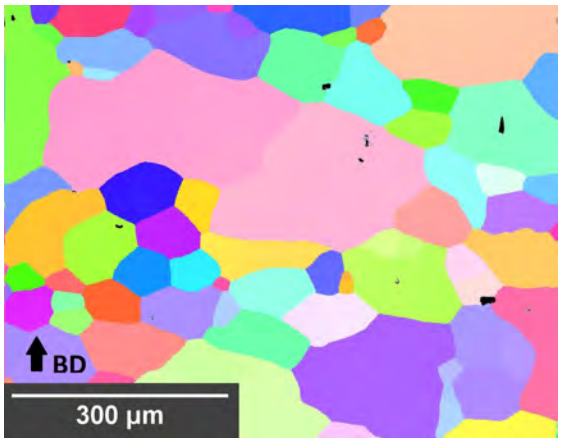

(e) W25Re Post-H Anneal, avg diameter: 56 μm

Figure 27. EBSD Maps for Selected Alloy Compositions. Images were taken from the side of the polished sample cubes, with the build direction increasing in the vertical direction. Grain sized measured using image analysis software and averaged over 20 measurements.

To study the grain structure, shape, size, and orientation, EBSD maps were generated for each composition. All maps were taken from polished surfaces of 10mm cubes printed with 50 micron hatch spacing, 200 W laser power and optimal laser speed for crack reduction. The EBSD maps for each composition in Figure 27 show a stark contrast between W, WRe, and heat treated WRe alloys. Both W and W5Re show columnar grain structures

5.2 Powder Composition Effect

As expected [4,6], higher concentrations of rhenium ductilize tungsten by lowering the DBTT. This is shown to reduce, but not eliminate completely, microcracking in the AM W25Re samples as compared to both the W and W5Re samples. See the Chapter 4 composition collages in Figures 25 and 26 for an SEM imagery comparison of all alloy compositions. Notably, in pure tungsten, microcracks seem to connect between microvoids in the print surface. The residual stresses in the tungsten matrix are increased by interstitial oxygen content in the lattice structure [18, 30].

5.2.1 Rhenium Content

The 25% rhenium printed parts appeared to have less microcracking than the 5% rhenium content parts, which in turn had less than pure tungsten. This result was expected based on the long history of WRe alloys in traditional manufacturing [6, 30, 46]. Alloying with rhenium lowers the DBTT of tungsten by increasing solubility of interstitial impurities and reducing the embrittlement of grain boundaries and lowering Peierls stress [27]. This increase in ductility was shown in the tensile tests. Tensile tests for the pure tungsten parts were not attempted; the parts were so brittle the specimens would fracture at the start of testing with an unmeasurable pressure below 10 MPa. However, tensile tests for AM W25Re showed average

UTS values of around 250 MPa, which is approximately 35% of the yield strength of traditionally manufactured W25Re at room temperature. Further work is needed to test at high temperatures to discover whether the same temperature-strength relationships are similar for AM and traditionally manufactured WRe parts. W5Re has the best creep resistance of WRe alloys [25], while W25Re is the near the solubility limit and offers the lowest DBTT of WRe alloys [6, 46]. Of these varying content amounts, two AM compositions stood out. As stated, W25Re was very easy to print, particularly on copper build surfaces, with no lifting from the print bed and minimal failed prints. This combined with heat treatment processes (discussed later) offer promising high temperature strength applications. The other promising composition was W25Re1HfC.

5.2.2 Hafnium Carbide Content

W25Re1HfC had the highest density produced of all alloy compositions at 97% theoretical density, as well as a microstructure free of cracks. Several large macroscopic cracks occurred at 2-5 mm height intervals, as well as build plate lifting occurring on all tested build plate materials. The visible cracks but nonexistent microcracking suggests rapidly changing thermal stress, not the DBTT, is responsible for both cracking and lifting. This material was 150 VH harder than the W25Re without HfC. Furthermore, Focused Ion Beam (FIB) imagery of the W25Re1HfC print specimens show that this microcracking elimination is not just a surface phenomena.

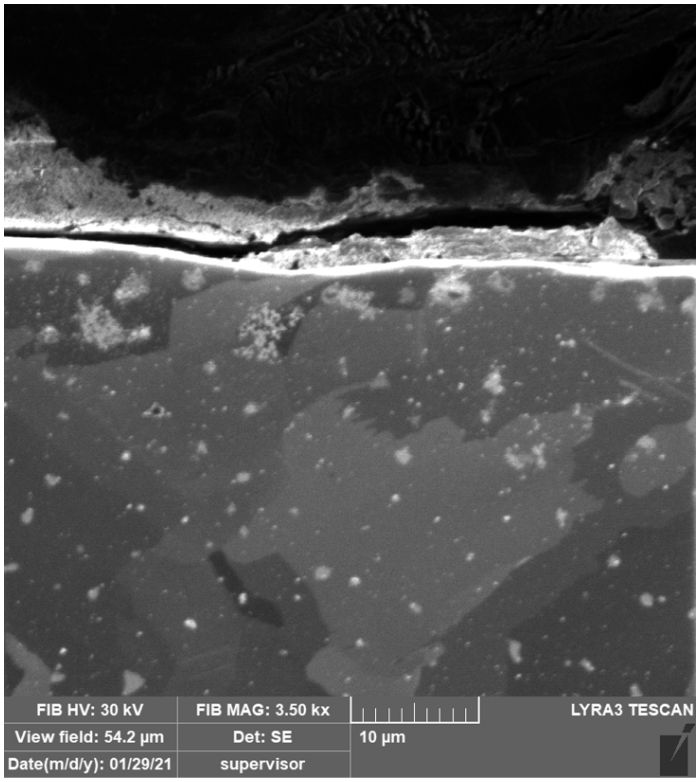

Figure 28. FIB imaging showing crack free region under surface

5.3 Printing Parameter Effects

The largest parameter which affected AM WRe density was laser power. The laser scan speed could be slowed to simulate powers over the Mlab AM machine's maximum 200 W laser power, but scan speeds, scan patterns, and the material properties of the build chamber and WRe powder mixture led to theoretical identical E_v values, but which produced different print quality results. Thus, 200 W was left as the optimal laser power for WRe and WReHfC alloys in this work. Further work is needed to discover the optimal laser power in AM machines with higher maximum laser powers. Most alloy compositions had a range of laser scan speeds that would produce similar results. W25Re and W25Re1HfC produced usable parts on copper build surfaces with 400 mm/s laser scan speed. Hatch spacing showed no significant effect between 25 μm, 50 μm, and 75 μm. A possible slight peak UTS for W25Re tensile bars

was noticed using 50 μm, so this was chosen as the optimal hatch spacing. Laser scan strategies for the W25Re showed negligible effect on cracking. Vertically printed tensile bar specimens were more prone to crack through the gauge section, but visibly defect-free specimens were stronger than their horizontally printed versions. However the horizontally printed versions showed less variability in UTS.

5.4 Post-Processing Effects

The heat treatments showed extreme promise. The hydrogen annealing produced W25Re specimens with an average UTS of 660 MPa at room temperature, while for HIP treated specimens this was 496 MPa. Both results are impressive and warrant further research.

Figure 27 shows EBSD grain maps of different alloy compositions. Each is strikingly different. The W produces large, columnar grains. Adding 5% rhenium reduces the size of these grains, but they still retain column structure with the build direction. W25Re produces small irregularly shaped grains. These likely have weak grain boundaries, which are strengthened during a heat treatment process. The post-HIP specimen microstructure contains small polygonized grains typical of cold-rolled tungsten or tungsten rhenium. The hydrogen annealed specimens contain large grains by comparison, also very polygonized. The larger grain size should lead to weaker strengths and lower ductility, but this is likely offset by the much lower interstitial oxygen in the lattice structure from the reducing hydrogen environment during annealing. Oxygen reduction is proven to play the biggest role in producing defect-free, strong AM tungsten alloys.

5.5 Summary

For WRe and WReHfC AM parts, print parameters are important to optimize, but successful parts are likely more defined by chemistry and build environment than by process improvement. These studies have shown it is easy to degrade material properties with sub-optimal parameters, but not yet possible to achieve traditionally manufactured material properties using only AM machine print parameters.

VI. Conclusions and Recommendations

6.1 Conclusions

Tungsten and tungsten alloys remain one of the few material system choices for extreme high temperature structural applications, especially in uses where higher thermal conductivity is desirable. When tungsten alloys are combined with additive manufacturing, previously impossible geometries can be fabricated. Many geometries, such as nozzles, have high surface areas. Traditional subtractive machining would require large amounts of bulk material. While metal powders generally cost more to manufacture, this effect is reduced when the raw material is expensive as well as requiring expensive machining. Rhenium is such a material; being able to add the exact amount of rhenium into the manufactured part is a benefit to AM. W25Re, W5Re, or W25Re1HfC AM parts printed on unexplored build plates such as copper, combined with heat treatment techniques such as HIP or hydrogen annealing offer usable parts at room temperature, and likely retain some strength at extremely high temperatures up to 2300 deg C. Removing oxygen from the products at all stages of production remains an essential step to creating defect-free parts.

6.2 Future Work

The work here puts forth many possibilities to improve additively manufactured tungsten parts. These ideas are mainly centered around removing oxygen content or its effects from the printed parts during printing. This could be done by varying alloy composition as with rhenium to improve solubility, by reducing oxygen's effect on the DBTT by varying temperature regimes, and by removing oxygen all together either from the build environment or with a post-processing heat treatment.

- High temperature mechanical tests of WRe and WReHfC with and without heat treatments to see if the percentage of strength holds at higher temperatures.
- Explore whether HIP can produce parts as strong as hydrogen annealing by using an argon-hydrogen mixture, or simply increase the time spent in HIP.
- Expand on the build plate parameters with different materials and heated build plates to reduce thermal shock stresses during solidification following laser melting.
- Change the AM machine gas mixture from pure argon to hydrogen or an argon-hydrogen mixture to form an oxygen reducing environment to reduce the embrittling effect of oxygen.
- Explore the alloy space further with other known useful elements including Mo, Ti, and C which may serve the purposes of oxygen scavenging and ductility, though this parameter space is largely unexplored.

Metal additive manufacturing pushes the boundaries of both materials science and engineering design. Advances in additive technologies will produce a compounding effect in many other industry, medical, military, and civil uses.

Appendix A. Sample Prep Procedure

William “Tommy” Cissel

Cobalt- and Nickel-based Superalloy sample preparation.

The procedures list are a combination of generic steps for the preparation of Cobalt- and Nickel-based Superalloys.

Sectioning:

The use of a high speed saw with an Aluminum Oxide Rubber Bonded blade at 3000 rpms, a feed rate 0.05” /min with a low force was used in the sectioning process.

Options are below:

Low speed Saw: HC Diamond Blade. Range 150 – 300 RPM (Speed range and force is dependent on size, thickness and density).

High Speed Saw: Aluminum Oxide Rubber Bonded. Range 2800 – 3000 RPM, 0.05”/min, low force.

Mounting:

The use of a conductive phenolic resin was used for various SEM analysis procedures. Currently, Struars PolyFast is used and cured with a hot mounting press. If light microscopy is the only unit used for analysis, a non-conductive phenolic, Buehler EpoMet, should be used.

	Resin Type	Heating Temp	Heating Pressure	Heating Time	Cooling Time	Cooling Rate
1	PolyFast	180°C	4800 psi	3.5	1.5	High
1	EpoMet	180°C	4800 psi	3.5	1.5	High

printed 2/7/2021

Grinding/Polishing:

Silicon Carbide papers, Buehler Apex DGD and TriDent cloths were used for the preparation of the specimens. The use of colloidal silica (SiO_2) is labeled for final polish; however, depending of the alloy, a combination of SiO_2 and alumina (Al_2O_3) can be used to chemically polish and etch the surface, revealing the macrostructure. Though, SiO_2 / Al_2O_3 should not be used if performing EBSD analysis.

A Buehler EcoMet 250 was used to grind and polish the samples. The settings used for each step can be found in Table 1.

Cleaning was performed before each step. After each grinding step, the samples were rinsed with water. After each polishing step, the samples were rinsed with isopropanol and water and hand washed to remove any colloidal particles from the surface.

After the 1 μm Diamond polishing step, the samples were cleaned as stated above, then rinsed with ethanol and dried with hot air. The samples were then mounted in a weighted holder, labeled, and polished in the Vibromet containing 0.05 μm SiO_2 solution overnight.

The following techniques show the parameter for a semi-auto unit, though could be modified to support "hand" grinding and polishing by eliminating the specifics of "Head Speed" and "Pressure" if desired.

Post-Vibromet Treatment:

After the sample was allowed to be polished in the vibromet using 0.05 μm SiO_2 solution, the sample was immediately rinsed with water. The sample was then immersed in a beaker containing acetone and sonicated for 5-10 minutes. The sample was then moved to a beaker containing isopropanol, where it was again sonicated for 5-10 minutes. It was then rinsed with distilled water, coated with ethanol or isopropanol, and dried.

	Surfac e	Grit Size	Time (Estimated)	Spin Type	Base Speed	Head Speed	Pressure
1	SiC Paper	240	5 min to start, Repeat until planar	Complimentary	300 rpm	50 rpm	5 lbs
2	SiC Paper	320	4 min	Complimentary	300 rpm	50 rpm	5 lbs
3	SiC Paper	400	3 min	Complimentary	150 rpm	50 rpm	5 lbs
4	SiC Paper	600	3 min	Complimentary	150 rpm	50 rpm	5 lbs
5*	Gold Label	9 µm Diamond	3 min	Contra	150 rpm	50 rpm	4 lbs
6	TriDent	3 µm Diamond	2 min	Complimentary	150 rpm	50 rpm	4 lbs
7	TriDent	1 µm Diamond	2 min	Complimentary	150 rpm	50 rpm	4 lbs

Table 1: Grinding/Polishing steps using a semi-automatic grinder polisher. *Note: The water should not be on during the polishing steps, and samples should be rinsed with ethanol to remove additional diamond suspension grit.

Appendix B. Experimental Test Points

Heat Treat	Specimen	Direction	Build Direction	Hatch	Speed	Ev	Ev	Width (mm)	Thick (mm)	Max Force	Stress MPa)	Notes
1.00	1.00	Horizontal	1.00	75	200	889	889	3.26	5.79	4555.49	241.3452059	
1.00	2.00	Horizontal	1.00	75	200	889	889	3.27	5.79	4388.03	231.9631177	
1.00	3.00	Horizontal	1.00	75	200	889	889	3.32	5.76	3756.79	196.4517654	
1.00	4.00	Horizontal	1.00	75	1000	178	178	3.20	5.76	4825.87	262.4576683	
1.00	5.00	Horizontal	1.00	75	1000	178	178	3.22	5.78	3803.16	204.3434578	
1.00	6.00	Horizontal	1.00	75	1000	178	178	3.21	5.71	4715.78	257.2838655	
1.00	1.00	Horizontal	1.00	75	800	222	222	3.23	5.94	5332.90	277.9549885	
1.00	2.00	Horizontal	1.00	75	800	222	222	3.21	5.93	5302.80	278.5771698	
1.00	3.00	Horizontal	1.00	75	800	222	222	3.22	5.92	5393.80	282.954927	
1.00	4.00	Horizontal	1.00	75	400	444	444	3.25	5.87	7728.32	405.1012135	
1.00	5.00	Horizontal	1.00	75	400	444	444	3.30	5.85	4429.11	229.4281689	
1.00	6.00	Horizontal	1.00	75	400	444	444	3.23	5.83	4845.18	257.299683	
1.00	1.00	Horizontal	1.00	50	1000	267	267	3.23	5.95	3263.70	342.519809	Seemed like good test
1.00	2.00	Horizontal	1.00	50	800	333	333	3.25	5.97	2854.00	295.6746957	Unknown if force fluctuating
1.00	3.00	Horizontal	1.00	50	600	444	444	3.28	5.96	2317.80	238.7318721	Force sensor fluctuating rapidly, may not be good test
1.00	4.00	Horizontal	1.00	75	600	296	296	3.26	3.00	2066.00	211.2474438	Switched Machines, Good Test
1.00	5.00	Horizontal	1.00	25	800	667	667	3.25	2.99	2389.00	245.8451248	Good Test
1.00	6.00	Horizontal	1.00	25	1000	533	533	3.22	2.98	2589.00	269.8111634	Good Test
1.00		Vertical	2.00	50	400	667	667	2.77	2.76	2328	304.5047873	
1.00		Vertical	2.00	50	400	667	667	2.92	2.89	2574	305.019671	
1.00		Vertical	2.00	50	700	381	381	2.87	2.84	3149	386.3424449	
1.00		Vertical	2.00	50	700	381	381	2.84	2.88	2947	360.3041862	
1.00		Vertical	2.00	50	1000	267	267	2.78	2.86	768	96.59405343	
1.00		Vertical	2.00	50	1000	267	267	2.79	2.85	2487	312.7711752	
1.00		Vertical	2.00	50	1000	267	267	2.74	2.58	2096	296.497482	
1.00		Vertical	2.00	50	1000	267	267	2.78	2.85	84	10.60204468	
1.00		Vertical	2.00	50	1000	267	267	2.79	2.85	178	22.38571339	
1.00		Vertical	2.00	50	400	667	667	2.92	2.89	0	0	Broke Before Test
1.00		Vertical	2.00	50	700	381	381	2.87	2.83	0	0	Broke Before Test
2.00		Annealed	3.00	50	1000	267	267	2.42	2.69	4565	701.2504224	Annealed
2.00		Annealed	3.00	50	1000	267	267	2.27	2.66	3837	635.4542745	Annealed
2.00		Annealed	3.00	50	1000	267	267	2.26	2.68	3903	644.399683	Annealed
3.00		HIP	4.00	50	1000	267	267	2.31	2.69	3092	497.5941035	HIP
	W25Re1HfC		5.00	50	1000	267	267	2.14	3	847	131.9314642	W25Re1HfC

Appendix C. Chemistry and Microhardness Report

LABORATORY REPORT 120180

TO: Major Ryan A. Kemnitz DATE: January 25, 2021

COMPANY: AFIT/ENY RECEIVED: December 18, 2020
Bldg. 640 Room 341C
Wright-Patterson AFB, OH

IDENTIFICATION: Chemistry Samples (7 each); Microhardness Samples (9 each).

Chemistry Samples:

- Sample# 1 W-25 Re; 7-7-20; powder;
- Sample# W-4% HFC; 25% Re; 9.25; powder;
- Sample# HFC Only; powder;
- Sample# Blanks; #1, #2, #3;
- Sample# Buttons.

Microhardness Samples:

- Sample# 12-3 (Baseline);
- Sample# 15-50 (Baseline);
- Sample# 14-6 (Post – HIP);
- Sample# 15-50 (Post – HIP);
- Sample# 14-5 (Post – 2400C);
- Sample# 14-14 (Post – 2400);
- Sample# +H4;
- Sample# +H42;
- Sample# W600.

INTRODUCTION: Seven (7) samples, as identified above, were submitted for oxygen and carbon analyses and nine (9) samples, as identified above, were submitted for microhardness evaluation.

TEST PROCEDURES: Oxygen was evaluated by combustion method in accordance with ASTM Standard E1019 using a LECO ONH 836 gas analyzer. Carbon was evaluated by the combustion method in accordance with ASTM Standard E1019 using a LECO CS200 Carbon/Sulfur Analyzer. Microhardness evaluation was accomplished in accordance with ASTM Standard E384 using a Mitutoyo 5104 MicroMet hardness tester with a 500-gram load for 15 second load application period.

TEST RESULTS:

I. Chemical Analysis:

Element (wt %)	1 W-25 Re; 7-7-20	W-4% HFC; 25% Re	HFC Only	Blank# 1	Blank# 2	Blank# 3	Buttons
Carbon	0.003	0.23	6.98	0.62	0.003	0.007	0.017
Oxygen	0.266	0.132	0.951	0.022	0.004	0.094	0.034

II. Microhardness Evaluation:

Location	Sample# 12-3 Baseline		Sample# 15-50 Baseline		Sample# 14-6 Post – HIP	
	HV_{500}	HRC	HV_{500}	HRC	HV_{500}	HRC
#1	404.5	41.5	426.2	43.3	428.8	43.5
#2	470.5	47.0	466.6	46.7	467.1	46.7
#3	413.8	42.2	473.8	47.2	433.7	44.0
#4	421.6	42.9	436.3	44.2	478.6	47.6
#5	441.7	44.6	441.6	44.6	465.5	46.6
Avg.	430.4	43.6	448.9	45.2	454.7	45.7

Location	Sample# 15-50 Post – HIP		Sample# 14-5 Post – 2400C		Sample# 14-14 Post – 2400	
	HV_{500}	HRC	HV_{500}	HRC	HV_{500}	HRC
#1	449.0	45.2	423.3	43.0	458.6	46.0
#2	444.7	44.9	440.8	44.6	474.6	47.3
#3	455.7	45.8	451.2	45.4	459.5	46.1
#4	413.6	42.1	425.1	43.2	403.9	41.2
#5	449.5	45.3	411.4	41.9	462.8	46.4
Avg.	442.5	44.7	430.4	43.6	451.9	45.4

Location	Sample# +H4		Sample# +H42		Sample# W600	
	HV_{500}	HRC	HV_{500}	HRC	HV_{500}	HRC
#1	595.2	55.0	591.2	54.8	426.9	43.4
#2	583.7	54.4	584.7	54.4	386.9	39.5
#3	648.1	57.8	580.3	54.2	394.0	40.2
#4	605.6	55.6	582.3	54.3	364.4	37.2
#5	592.5	54.5	586.2	54.5	364.4	37.2
Avg.	605.0	55.5	584.9	54.4	387.3	39.5

HV_{500} = Vickers Hardness Scale with 500-gram Load
HRC = Rockwell C Hardness Scale

Craig A. Riviello
Director of Testing Services

Bibliography

1. W. D. Klopp, "Review of ductilizing of Group VIA elements by rhenium and other solutes," *NASA Technical Note, D-4955, Lewis Research Center Cleveland, Ohio*, no. December, pp. 1–37, 1968.

2. C. C. Eckley and R. A. Kemnitz, "Investigation of Varying Scanning Strategy on SLM of," 2020.

3. T. Leonhardt, "Properties of tungsten-rhenium and tungsten-rhenium with hafnium carbide," *Jom*, vol. 61, no. 7, pp. 68–71, 2009.

4. E. Lassner and W.-D. Schubert, *Element Tungsten: Its Properties*, 1st ed. New York: Kluwer Academic / Plenum Publishers, 1999.

5. D. Rupp and E. Gaganidze, "Fracture Mechanical Properties of Tungsten Alloys," in *CRPP_EFPL Fusion Technology Materials*. Villigen PSI, Switzterlkand: Karlsruher Institut für Technologie, 2010, p. 28.

6. C. Ren, Z. Fang, M. Koopman, B. Butler, J. Paramore, and S. Middlemas, "Methods for improving ductility of tungsten - A review," *International Journal of Refractory Metals and Hard Materials*, vol. 75, pp. 170–183, 9 2018. [Online]. Available: https://www.sciencedirect.com/science/article/abs/pii/S0263436818300659

7. C. Hull, "Apparatus for production of three dimensional objects by Stereolithography," 1986.

8. D. Wang, Z. Wang, K. Li, J. Ma, W. Liu, and Z. Shen, "Cracking in laser additively manufactured W: Initiation mechanism and a suppression approach

by alloying," *Materials and Design*, vol. 162, pp. 384–393, 2019. [Online]. Available: https://doi.org/10.1016/j.matdes.2018.12.010

9. B. Vrancken, W. E. King, and M. J. Matthews, "In-situ characterization of tungsten microcracking in Selective Laser Melting," *Procedia CIRP*, vol. 74, pp. 107–110, 2018. [Online]. Available: https://doi.org/10.1016/j.procir.2018.08.050

10. R. Kemnitz, "Tungsten Results from Others Zhou : Balling phenomena in selective laser melted tungsten," no. March, pp. 1–9, 2020.

11. A. Luo, D. L. Jacobson, and K. S. Shin, "Tensile properties of tungsten-3.6% rhenium-0.4% hafnium carbide above 0.5 Tm," *Scripta Metallurgica*, vol. 23, no. 3, pp. 397–400, 1989.

12. F. Romei and A. Grubisic, "Numerical study of a novel monolithic heat exchanger for electrothermal space propulsion," *Acta Astronautica*, vol. 159, pp. 8–16, 2019. [Online]. Available: http://www.sciencedirect.com/science/article/pii/S0094576518315182

13. Y. Zhong, L. E. Rännar, L. Liu, A. Koptyug, S. Wikman, J. Olsen, D. Cui, and Z. Shen, "Additive manufacturing of 316L stainless steel by electron beam melting for nuclear fusion applications," *Journal of Nuclear Materials*, vol. 486, pp. 234–245, 2017.

14. L. B. Zhang, Y. Q. Peng, J. B. Zhou, R. H. Zhang, S. Chen, and X. F. Yang, "Tungsten-rhenium thermocouple sensor for in-situ ultra-high temperature measurement of hypersonic aircraft surface," *Proceedings of the International Instrumentation Symposium*, 2014.

15. S. Wen, C. Wang, Y. Zhou, L. Duan, Q. Wei, S. Yang, and Y. Shi, "High-density tungsten fabricated by selective laser melting: Densification,

microstructure, mechanical and thermal performance," *Optics and Laser Technology*, vol. 116, no. December 2018, pp. 128–138, 2019. [Online]. Available: https://doi.org/10.1016/j.optlastec.2019.03.018

16. C. Tan, K. Zhou, W. Ma, B. Attard, P. Zhang, and T. Kuang, "Selective laser melting of high-performance pure tungsten: parameter design, densification behavior and mechanical properties," *Science and Technology of Advanced Materials*, vol. 19, no. 1, pp. 370–380, 2018. [Online]. Available: http://doi.org/10.1080/14686996.2018.1455154

17. K. Li, D. Wang, L. Xing, Y. Wang, C. Yu, J. Chen, T. Zhang, J. Ma, W. Liu, and Z. Shen, "Crack suppression in additively manufactured tungsten by introducing secondary-phase nanoparticles into the matrix," *International Journal of Refractory Metals and Hard Materials*, vol. 79, pp. 158–163, 2019. [Online]. Available: https://doi.org/10.1016/j.ijrmhm.2018.11.013

18. Cole N C; Gilliland R G; Slaughter G M, "Weldability of tungsten and its alloys," *Weld J (NY)*, vol. 50, no. 9, 1971.

19. J. Daintith, *The Facts On File Dictionary of Chemistry*, 4th ed. Facts on File, 2005.

20. Z. S. Levin, A. Srivastava, D. C. Foley, and K. T. Hartwig, "Fracture in annealed and severely deformed tungsten," *Materials Science and Engineering: A*, vol. 734, no. December 2017, pp. 244–254, 2018. [Online]. Available: http://www.sciencedirect.com/science/article/pii/S0921509318306440https://doi.org/10.1016/j.msea.2018.05.004

21. S. Antusch, D. E. Armstrong, T. B. Britton, L. Commin, J. S. Gibson, H. Greuner, J. Hoffmann, W. Knabl, G. Pintsuk, M. Rieth, S. G. Roberts, and

T. Weingaertner, "Mechanical and microstructural investigations of tungsten and doped tungsten materials produced via powder injection molding," *Nuclear Materials and Energy*, vol. 3-4, pp. 22–31, 2015. [Online]. Available: http://dx.doi.org/10.1016/j.nme.2015.04.002

22. J. Roesler, H. Harders, and M. Baeker, *Mechanical Behavior of Engineering Materials*, 2006.

23. J. Diaz, "Pure rhenium metal," *IEEE Potentials*, vol. 15, no. 1, pp. 37–39, 1996. [Online]. Available: http://ieeexplore.ieee.org/document/481375/

24. B. Gludovatz, S. Wurster, A. Hoffmann, and R. Pippan, "Fracture toughness of polycrystalline tungsten alloys," *International Journal of Refractory Metals and Hard Materials*, vol. 28, no. 6, pp. 674–678, 11 2010. [Online]. Available: http://dx.doi.org/10.1016/j.ijrmhm.2010.04.007https://linkinghub.elsevier.com/retrieve/pii/S0263436810000594

25. J. Webb, S. Gollapudi, and I. Charit, "An overview of creep in tungsten and its alloys," *International Journal of Refractory Metals and Hard Materials*, vol. 82, no. February, pp. 69–80, 2019. [Online]. Available: https://doi.org/10.1016/j.ijrmhm.2019.03.022

26. W. D. Klopp, "A review of chromium, molybdenum, and tungsten alloys," *Journal of the Less Common Metals*, vol. 42, no. 3, pp. 261–278, 10 1975. [Online]. Available: https://www.sciencedirect.com/science/article/abs/pii/0022508875900466

27. P. L. Raffo, "Yielding and fracture in tungsten and tungsten-rhenium alloys," *Journal of the Less Common Metals*, vol. 17, no. 2, pp. 133–149, 2

1969. [Online]. Available: https://www.sciencedirect.com/science/article/abs/pii/0022508869900472

28. M. Garfinkle, "ROOM-TEMPERATURE TENSILE BEHAVIOR OF ¡100¿ ORIENTED TUNGSTEN SINGLE CRYSTALS WITH RHENIUM IN DILUTE SOLID SOLUTION," *NASA-TN*, vol. D-3190, 1966.

29. A. Gilbert, "A fractographic study of tungsten and dilute tungsten-rhenium alloys," *Journal of The Less-Common Metals*, vol. 10, no. 5, pp. 328–343, 1966. [Online]. Available: http://www.sciencedirect.com/science/article/pii/0022508866901330

30. W. D. Kzopp, "REVIEW OF DUCTILIZING OF GROUP VIA ELEMENTS BY RHENIUM AND OTHER SOLUTES," Tech. Rep. [Online]. Available: https://ntrs.nasa.gov/search.jsp?R=19690005071

31. C. Jaffee, R.; Sims, "THE EFFECT OF RHENIUM ON THE FABRIGABILITY AND DUCTILITY OF MOLYBDENUM AND TUNGSTEN," p. 49, 1958. [Online]. Available: https://apps.dtic.mil/dtic/tr/fulltext/u2/156574.pdf

32. J. Reiser, J. Hoffmann, U. Jäntsch, M. Klimenkov, S. Bonk, C. Bonnekoh, M. Rieth, A. Hoffmann, and T. Mrotzek, "Ductilisation of tungsten (W): On the shift of the brittle-to-ductile transition (BDT) to lower temperatures through cold rolling," *International Journal of Refractory Metals and Hard Materials*, vol. 54, pp. 351–369, 1 2016. [Online]. Available: http://www.sciencedirect.com/science/article/pii/S0263436815301475https://linkinghub.elsevier.com/retrieve/pii/S0263436815301475

33. M. Yakout, M. A. Elbestawi, and S. C. Veldhuis, "A review of metal additive manufacturing technologies," *Solid State Phenomena*, vol. 278 SSP, pp. 1–14, 2018.

34. D. Herzog, V. Seyda, E. Wycisk, and C. Emmelmann, "Additive manufacturing of metals," *Acta Materialia*, vol. 117, pp. 371–392, 9 2016. [Online]. Available: https://linkinghub.elsevier.com/retrieve/pii/S1359645416305158

35. A. 52900:2015, "Standard Terminology for Additive Manufacturing – General Principles – Terminology," ASTM, Tech. Rep., 2015. [Online]. Available: http://compass.astm.org/EDIT/html_annot.cgi?ISOASTM52900+15

36. U. G. S., *Powder metallurgy technology*, 2002. [Online]. Available: https://books.google.cz/books/about/Powder_Metallurgy_Technology.html?id=04lT--Sbxb4C&redir_esc=y

37. A. S. Baskoro, S. Supriadi, and Dharmanto, "Review on Plasma Atomizer Technology for Metal Powder," *MATEC Web of Conferences*, vol. 269, p. 05004, 2019.

38. R. M. German, *Powder Metallurgy Science.*, 1984.

39. Grenier, "Plasma atomization gives unique spherical powders," *Metal Powder Report*, vol. 52, no. 11, pp. 34–37, 1997.

40. C. Y. Yap, C. K. Chua, Z. L. Dong, Z. H. Liu, D. Q. Zhang, L. E. Loh, and S. L. Sing, "Review of selective laser melting: Materials and applications," *Applied Physics Reviews*, vol. 2, no. 4, p. 041101, 12 2015. [Online]. Available: http://aip.scitation.org/doi/10.1063/1.4935926

41. A. Iveković, N. Omidvari, B. Vrancken, K. Lietaert, L. Thijs, K. Vanmeensel, J. Vleugels, and J. P. Kruth, "Selective laser melting of tungsten and tungsten

alloys," *International Journal of Refractory Metals and Hard Materials*, vol. 72, no. December 2017, pp. 27–32, 2018.

42. A. Iveković, M. L. Montero-Sistiaga, K. Vanmeensel, J.-P. Kruth, and J. Vleugels, "Effect of processing parameters on microstructure and properties of tungsten heavy alloys fabricated by SLM," *International Journal of Refractory Metals and Hard Materials*, vol. 82, pp. 23–30, 8 2019. [Online]. Available: https://linkinghub.elsevier.com/retrieve/pii/S0263436819300216

43. M. K. Banerjee, *Fundamentals of Heat Treating Metals and Alloys*. Elsevier Ltd., 2017, vol. 2-3. [Online]. Available: http://dx.doi.org/10.1016/B978-0-12-803581-8.09185-2

44. ASTM International, "ASTM B962-17, Standard Test Methods for Density of Compacted or Sintered Powder Metallurgy (PM) Products Using Archimedes' Principle," ASTM, West Conshohocken, PA, Tech. Rep., 2017. [Online]. Available: www.astm.org

45. ——, "ASTM E8 / E8M-16ae1, Standard Test Methods for Tension Testing of Metallic Materials," ASTM, West Conshohocken, PA, Tech. Rep., 2016. [Online]. Available: www.astm.org

46. W. D. Klopp, W. R. Witzke, and P. L. Raffo, "Mechanical Properties of Dilute Tungsten-Rhenium Alloys," *Nasa Technical Note*, vol. D-3483, no. September, pp. 1–32, 1966.

REPORT DOCUMENTATION PAGE

Form Approved
OMB No. 0704–0188

1. REPORT DATE *(DD–MM–YYYY)*	2. REPORT TYPE	3. DATES COVERED *(From — To)*
21–03–2021	Master's Thesis	Sept 2019 — Mar 2021

4. TITLE AND SUBTITLE

Improving Manufacturability and Reducing Cracking in Additively Manufactured Tungsten Alloys

5a. CONTRACT NUMBER

5b. GRANT NUMBER

5c. PROGRAM ELEMENT NUMBER

6. AUTHOR(S)

Fassio, Christopher P., Captain, USAF

5d. PROJECT NUMBER

5e. TASK NUMBER

5f. WORK UNIT NUMBER

7. PERFORMING ORGANIZATION NAME(S) AND ADDRESS(ES)

Air Force Institute of Technology
Graduate School of Engineering an Management (AFIT/EN)
2950 Hobson Way
WPAFB OH 45433-7765

8. PERFORMING ORGANIZATION REPORT NUMBER

AFIT-ENY-MS-21-M-299

9. SPONSORING / MONITORING AGENCY NAME(S) AND ADDRESS(ES)

Air Force Research Laboratory

10. SPONSOR/MONITOR'S ACRONYM(S)

AFRL

11. SPONSOR/MONITOR'S REPORT NUMBER(S)

12. DISTRIBUTION / AVAILABILITY STATEMENT

DISTRIBUTION STATEMENT A:
APPROVED FOR PUBLIC RELEASE; DISTRIBUTION UNLIMITED.

13. SUPPLEMENTARY NOTES

14. ABSTRACT

Additively Manufactured tungsten suffers from low (<95%) densities due to high concentrations of microcracks as the printed layers cool past tungsten's high ductile to brittle transition temperature. In this study, tungsten-rhenium and tungsten rhenium hafnium carbide compositions were evaluated on density and tensile strength. In addition to varying the compositions of each alloy, printing parameters and post-processing methods were also compared. Print parameters varied for all compositions on an MLab 200R Cusing included the laser scan strategy, hatch spacing, scan speed, laser power, and print bed material. Post processing techniques of the WRe compositions included hot isostatic pressing and hydrogen annealing treatments. In particular, two combinations achieved high density (>97%) indicating a reduction in micro-cracking: W25Re which underwent H annealing, and W25Re1HfC as-printed. In both cases the mechanism was likely oxygen impurities being scavenged, either by hydrogen or carbon. The H annealed W25Re tensile bar achieved a 701 MPa room temperature ultimate tensile strength. Scanning Electron Microscope images of the annealed W25Re and the as-printed W25Re1HfC show no microcracks. This was further confirmed on the W25Re1HfC using Focused Ion Beam imaging techniques. However, the reduction in microcracking in the latter led to a buildup in thermal stresses during printing, causing both lifting from the print bed, and macro sized cracks through the printed part approximately every 5mm in print height. Lifting was reduced by using a copper build plate, with an "island" laser scan strategy.

15. SUBJECT TERMS

Additive Manufacturing, Tungsten Alloys, LPBF

16. SECURITY CLASSIFICATION OF:			17. LIMITATION OF ABSTRACT	18. NUMBER OF PAGES	19a. NAME OF RESPONSIBLE PERSON
a. REPORT	b. ABSTRACT	c. THIS PAGE			Ryan Kemnitz, AFIT/ENY
U	U	U	UU	72	19b. TELEPHONE NUMBER *(include area code)* (937) 255-3636 x4775; ryan.kemnitz@afit.edu